Journal of Computational Physics 361 (2018) 56–81

Contents lists available at ScienceDirect

Journal of Computational Physics

www.elsevier.com/locate/jcp

Simulations of viscous and compressible gas–gas flows using high-order finite difference schemes

M. Capuano *, C. Bogey, P.D.M. Spelt

Laboratoire de Mécanique des Fluides et d'Acoustique, UMR CNRS 5509, Université de Lyon, France

ARTICLE INFO

Article history:
Received 14 September 2017
Received in revised form 9 January 2018
Accepted 27 January 2018
Available online xxxx

Keywords:
Finite differences
High-order
Multi-component flows
Interface
Viscous
Compressible

ABSTRACT

A computational method for the simulation of viscous and compressible gas–gas flows is presented. It consists in solving the Navier–Stokes equations associated with a convection equation governing the motion of the interface between two gases using high-order finite-difference schemes. A discontinuity-capturing methodology based on sensors and a spatial filter enables capturing shock waves and deformable interfaces. One-dimensional test cases are performed as validation and to justify choices in the numerical method. The results compare well with analytical solutions. Shock waves and interfaces are accurately propagated, and remain sharp. Subsequently, two-dimensional flows are considered including viscosity and thermal conductivity. In Richtmyer–Meshkov instability, generated on an air–SF6 interface, the influence of the mesh refinement on the instability shape is studied, and the temporal variations of the instability amplitude is compared with experimental data. Finally, for a plane shock wave propagating in air and impacting a cylindrical bubble filled with helium or R22, numerical Schlieren pictures obtained using different grid refinements are found to compare well with experimental shadowgraphs. The mass conservation is verified from the temporal variations of the mass of the bubble. The mean velocities of pressure waves and bubble interface are similar to those obtained experimentally.

1. Introduction

Gas–gas flows with strong effects of compressibility are encountered in various areas, from astrophysics, such as in supernova expansion where the fluid mixing is attributed to Richtmyer–Meshkov instability [6], to engineering, such as in supersonic combustion [45]. A main challenge for the simulation of these flows is that a deformable interface separates two fluids of different properties; furthermore, other discontinuities such as shock waves may arise. Specific concerns are that the computational methods capture such discontinuities accurately, without introducing spurious perturbations, and the accurate conservation of mass of the fluids.

Several methods have been developed for the simulation of a deformable interface [44,55]. These methods can be classified into interface-tracking and interface-capturing methods. Interface-tracking methods use an adaptive mesh, some points of which coincide with an interface [22,29,62], such that a mesh moves with the interface, possibly in conjunction with a uniform background mesh. These methods can be accurate, but difficulties arise during interface rupture or coalescence

* Corresponding author.
E-mail address: marion.capuano@doctorant.ec-lyon.fr (M. Capuano).

https://doi.org/10.1016/j.jcp.2018.01.047
0021-9991/

events, and implementation is involved for a three-dimensional geometry. In interface-capturing methods, a fixed mesh can be used. These methods simulate interface evolution by solving an advection equation for a scalar field.

A commonly-used type of interface-capturing methods is the level-set method [28,47,48], wherein the scalar field corresponds to the signed distance to the nearest interface. A drawback of that method is that, in order to maintain the level-set function as a signed-distance function, which is desirable for accurate determination of the normal vector of an interface, a reinitialisation step is commonly used, which may introduce significant mass errors. But some modern level-set methods appear not to be prone to this [58]. For compressible multi-component flows, level-set methods are frequently used in conjunction with a ghost-fluid method to apply interface conditions (e.g., [48]). It seems unclear, however, how such an approach could be generalized to simulate flows for viscous/conductive fluids, which is our objective here, as imposing the corresponding stress/energy jump conditions at interfaces would require further development, although such a formulation is available for incompressible flows [37].

An interesting alternative is to model an interface as a thin interfacial layer. Several approaches of this type have been developed for compressible flows. One of these is to use a single set of balance equations for a mixture; jumps in the value of fluid properties (such as those in the equation of state) occur in an interfacial layer. The system is then closed by an advection-type equation for (a function of) such a fluid property, or several of these, which can be put into conservative form upon combination with the mass balance equation for the entire mixture. The advected quantity is chosen such that interface conditions are satisfied accurately without introducing spurious oscillations in the pressure or in the fluid properties, when considering basic one-dimensional test problems. In particular, a judicious choice of an advected parameter reduces significantly deviations from a uniform pressure across an interface in a one-dimensional inviscid uniform flow; such pressure oscillations are specific to these multi-component systems (e.g., [1]). For the perfect gas equation of state, one advected quantity may be used (e.g., [1,2]). In all, a set of mixture relations used in the interfacial region should be consistent: that is, the primary variables and parameters in the equation of state should be determined in a consistent manner.

A second such approach is to resolve separately the balance equations for mass conservation, possibly also energy and momentum balance equations for each constituent. To obtain the local value of parameters in the equation of state inside an interfacial layer, these balance equations may have to be supplemented by a balance equation for the volume fraction of one of the constituents again such as to satisfy interface conditions in basic test problems (e.g., [4,15,54]). The formulation of an advection-type equation for the volume fraction is not straightforward however, and may require making assumptions (e.g., [34]). An approach based entirely on mass fractions has also been formulated [53].

This ‘diffuse’-interface type of model seems more suitable for systems with viscosity, wherein a discontinuity in tangential velocity does not have to be contended with. Accounting for conduction, and possibly for dependencies on temperature in the equation of state, requires reduction of errors in the temperature at basic one-dimensional tests, in addition to pressure errors, which has prompted further consideration of the formulation of mixture relations in view of errors in the temperature at basic one-dimensional tests, in addition to pressure errors (e.g., [7,34]).

These models have been formulated thus far mostly in a finite-volume methodology, in particular, using high-order WENO schemes. The objective of the present study is to develop high-order finite-difference methods for the simulation of viscous and compressible multi-component flows. These methods have initially been developed for aeroacoustic computations in order to provide negligible dissipation and dispersion errors [8,9]. In this work, the methods are adapted to the simulation of multi-component flows. High-order explicit centred finite difference schemes are used for spatial differentiation. In order to remove grid-to-grid oscillations, whose wavelength is equal to twice the mesh spacing, a centred selective filter is applied every time step, throughout the entire domain. A discontinuity-capturing methodology enables to capture various discontinuities such as deformable interfaces between two fluids or shock waves. The methods are employed to solve the Navier–Stokes equations associated with one advection equation governing the interface displacements [2,33]. In order to validate the present methods, three one-dimensional test cases are solved. The numerical results are compared with analytical solutions. Finally, the algorithm is employed to simulate two-dimensional viscous flows. Firstly, a Richtmyer–Meshkov instability generated on a post-shocked interface between air and sulphur hexafluoride (SF6) is investigated. Secondly, a plane shock wave propagating through air, impacting a cylindrical bubble filled with helium or chlorodifluoromethane (R22) gas is studied. The numerical results are compared with experimental solutions [24,30].

The present paper is organized as follows. The equations governing the test problems are given in Section 2. The numerical methods are detailed in Section 3. The one-dimensional and two-dimensional flows are presented, and solved in Sections 4 and 5, respectively. Concluding remarks are finally provided in Section 6.

2. Governing equations

2.1. Balance equations

Each of the two fluids considered does not occupy all space, so we shall make use of the volume fraction ϕ_α defined as that part of an infinitesimal volume occupied by fluid α, and denote by ρ_α the mass per unit volume of pure fluid α, and by e_α the internal energy per unit mass of pure fluid α. Pursuing a formulation of balance equations for an entire mixture, we note that the mixture density and internal energy are then

$$\rho = \sum_{\alpha} \phi_\alpha \rho_\alpha \,, \quad \rho e = \sum_{\alpha} \phi_\alpha \rho_\alpha e_\alpha \,, \tag{1}$$

and $\sum_\alpha \phi_\alpha = 1$. The velocity components are considered continuous for viscous systems without phase change, so a single velocity field is defined for both fluids; there is no relative motion between the fluids.

A single set of balance equations for the mixture mass, momentum and energy can be developed along standard arguments as follows (see, for instance, [14], albeit in the context of level-set methods). Consider a small volume of the mixture, possibly containing an interface between the two fluids. The contribution to a balance equation from the part of that volume occupied by fluid α is then merely the usual integrated balance equation for that fluid, but after replacing therein the density by $\phi_\alpha \rho_\alpha$, the internal energy per unit mass by $\phi_\alpha \rho_\alpha e_\alpha$ (with similar expressions for the stress tensor and heat flux); the same velocity $\mathbf{u}$ is used for both fluids. Taking the traction and heat flux to be continuous at interfaces (discussed further below), and using that the velocity component normal to an interface is the same as that of the velocity of each fluid (no phase change), the pre-constitutive governing equations for the gas–gas system can then be obtained upon using (1). In conservative form,

$$\begin{cases} \dfrac{\partial \rho}{\partial t} + \dfrac{\partial \rho u_i}{\partial x_i} = 0 \,, \\ \dfrac{\partial \rho u_i}{\partial t} + \dfrac{\partial \rho u_i u_j}{\partial x_j} = \dfrac{\partial \sigma_{ij}}{\partial x_j} \,, \\ \dfrac{\partial E}{\partial t} + \dfrac{\partial u_i E}{\partial x_i} = \dfrac{\partial}{\partial x_i}(\sigma_{ij} u_j) - \dfrac{\partial q_i}{\partial x_i} \,, \end{cases} \tag{2}$$

where $E = \rho |\mathbf{u}|^2/2 + \rho e$ is the total energy per unit volume. Although the fluid traction and heat flux are assumed to be continuous at interfaces, a discontinuity in either can be accounted for, as in the representation of surface tension in the continuous surface tension formulation [12]. We note further that the density and internal energy are *not* assumed to be continuous in this approach.

The procedure recalled above for obtaining the pre-constitutive mixture balance equations yields that the mixture stress tensor and heat flux appearing therein are defined as the averages of those in each fluid weighted by volume fraction. Adopting the Navier–Stokes–Fourier model, the constitutive relation for the stress tensor σ_{ij} is

$$\sigma_{ij} = -\left(p - \mu_b \frac{\partial u_k}{\partial x_k} \right) \delta_{ij} + \mu \left(\frac{\partial u_i}{\partial x_j} + \frac{\partial u_j}{\partial x_i} - \frac{2}{3} \frac{\partial u_k}{\partial x_k} \delta_{ij} \right) \,, \tag{3}$$

where δ_{ij} is the Kronecker delta, μ is the shear viscosity, μ_b is the bulk viscosity, and p is the thermodynamical pressure which differs from the mechanical pressure $p_m = p - \mu_b \nabla \cdot \mathbf{u}$. The heat flux is

$$q_i = -\lambda \frac{\partial T}{\partial x_i} \,, \tag{4}$$

where λ is the thermal conductivity and T is the temperature. Since these are averages weighted by volume fraction, we conclude that

$$p = \sum_{\alpha} \phi_\alpha p_\alpha \,, \tag{5}$$

and that weighting by volume fraction should also be used for the transport coefficients

$$\mu = \sum_{\alpha} \phi_\alpha \mu_\alpha \,, \quad \mu_b = \sum_{\alpha} \phi_\alpha \mu_{b\alpha} \,, \quad \lambda = \sum_{\alpha} \phi_\alpha \lambda_\alpha \,. \tag{6}$$

The empirical relations employed to estimate the values of these coefficients for each of the pure gases considered in the present study are given in Appendix A.

2.2. Equation of state

The mixture internal energy per unit volume can be developed starting with (1), upon using the definition of internal enthalpy for each fluid,

$$\rho e = \sum_{\alpha} \phi_\alpha \rho_\alpha e_\alpha = \sum_{\alpha} \phi_\alpha \rho_\alpha \left(h_\alpha - p_\alpha / \rho_\alpha \right) , \tag{7}$$

where h_α is the internal enthalpy per unit mass of pure fluid α. Invoking (5), we obtain

$$\rho e + p = \sum_{\alpha} \phi_\alpha \rho_\alpha h_\alpha . \tag{8}$$

The gases are assumed to be ideal, so the thermal expansion coefficient for each gas equals the inverse temperature and $dh_\alpha = c_{p,\alpha} dT$, where c_p is the specific heat at constant pressure. If we assume the gases to be perfect, c_p is constant (we discuss the more general case of imperfect ideal gases at the end of this subsection) and (8) becomes

$$\rho e + p = T \sum_\alpha \phi_\alpha \rho_\alpha c_{p,\alpha}. \tag{9}$$

It is at this point that we first have imposed the one remaining interface condition (not used in deriving the mixture balance equations), which is that the temperature be continuous at interfaces, i.e., $T_\alpha = T$.

To proceed further, we introduce the mass fraction of fluid α, denoted by Y_α, as the mass of fluid α per unit mixture mass, and after the mole fraction n_α as the amount of α (in moles) divided by the total amount of the mixture; both such that $\sum_\alpha n_\alpha = 1$ and $\sum_\alpha Y_\alpha = 1$. The ratio $n_\alpha M_\alpha / Y_\alpha$, where M_α is the molar mass of fluid α, is thus the mixture mass per unit amount of the mixture, which is defined as the mixture molar mass, denoted here by M [34]. Multiplying the resulting identity with $Y_\alpha/(M_\alpha M)$ and summing over the fluids then yields

$$\frac{1}{M} = \sum_\alpha \frac{Y_\alpha}{M_\alpha}\,, \tag{10}$$

where we have used that the mole fractions sum to unity. Multiplying with the universal gas constant R_u then yields the specific gas constant for the mixture as

$$R = \frac{R_u}{M} = \sum_\alpha Y_\alpha R_\alpha\,, \tag{11}$$

where $R_\alpha = R_u/M_\alpha$ is the specific gas constant of fluid α. For each ideal gas the specific gas constant satisfies Mayer's relation, $R_\alpha = c_{p,\alpha} - c_{v,\alpha}$, where $c_{v,\alpha}$ is the specific heat at constant volume for fluid α. This suggests $R = c_p - c_v$ with

$$c_p = \sum_\alpha Y_\alpha c_{p,\alpha}\,, \quad c_v = \sum_\alpha Y_\alpha c_{v,\alpha}\,. \tag{12}$$

Now, since the mass of fluid α per unit volume of mixture can then be written in two ways, which results in the identity

$$\phi_\alpha \rho_\alpha = \rho Y_\alpha\,, \tag{13}$$

we can write (9) as

$$\rho e + p = \rho c_p T. \tag{14}$$

This can be simplified further by using the equation of state for fluid α in (13) as

$$\phi_\alpha p_\alpha = \rho T Y_\alpha R_\alpha\,. \tag{15}$$

Summing over α then yields the mixture ideal gas law

$$p = \rho R T\,, \tag{16}$$

where we have used (11). The equation of state for the mixture is then, finally,

$$\rho e = \frac{p}{\gamma - 1}, \tag{17}$$

where $\gamma = c_p/c_v$ is the ratio of mixture specific heats.

Thus, to conclude, the mixture equation of state that accompanies the mixture balance equations is (17); the temperature can be obtained from (16), which requires the specific gas constant (11) of the mixture. We have also developed mixture relations for the mixture specific heats (12) and the molar mass (10). It remains, however, to determine the factor $1/(\gamma - 1)$ and the composition: the mass and volume fractions.

Although we have restricted ourselves here to perfect gases, it is straightforward to generalize the above for imperfect ideal gases: any dependency of $c_{p,\alpha}$ on temperature can readily be integrated to obtain the internal enthalpy, which merely gives an extra term in (9). For instance, for a linear dependency on temperature, $c_{p,\alpha} = c^0_{p,\alpha} + c^1_{p,\alpha} T$, this yields an extra term $(pT/R)\sum_\alpha Y_\alpha c^1_{p,\alpha}/2$ on the right-hand side of (17), which poses no further modelling difficulty. The cases considered herein involve temperature variations of a hundred Kelvin around ambient temperature, in which variations of specific heats are not significant, this generalisation is therefore not pursued herein.

In deriving (17), apart from ignoring a temperature dependence of the specific heats, we have only used continuity of temperature at interfaces, which is a physical interface condition; the pressure has not been assumed to be continuous here.

2.3. Interface evolution

It remains to determine the mixture composition: the mixture balance equations (2) with the constitutive relations (3) and (4) supplemented by the mixture equations of state (16)–(17) require the volume fraction in the mixture transport coefficients, and $1/(\gamma-1)$.

The composition of the mixture can be evolved using an advection-type equation for a scalar function $\chi(\mathbf{x},t)$ in non-conservative form

$$\frac{\partial \chi}{\partial t} + \mathbf{u}\cdot\nabla\chi = 0 \tag{18}$$

or, upon invoking mixture mass balance, in conservative form,

$$\frac{\partial \rho\chi}{\partial t} + \nabla\cdot(\mathbf{u}\rho\chi) = 0\,. \tag{19}$$

One possible choice for this scalar is the mass fraction of one of the fluids (say, $\chi = Y_1$), for which the transport equation is exact. The mixture specific heats and their ratio, alongside specific gas constant and molar mass then follow from the respective mixture relations derived in the previous subsection. On the other hand, this still leaves the determination of the volume fraction required for the mixture transport properties, (6); this can be obtained, but upon making a further modelling assumption such as ignoring a jump in pressure at interfaces: it then follows directly from the mass fraction through (13),

$$Y_\alpha = \phi_\alpha R/R_\alpha = \phi_\alpha M_\alpha/M\,. \tag{20}$$

We report on results obtained with this approach for an inviscid, non-conductive 1D system in Section 4.1.2.

A broader range of choices for the scalar function in the transport equation is identified by noting that most of the mixture relations developed in the previous subsection are averages weighted by the mass fractions; for example, the mixture specific heats, and the ratio of specific heats. Since each mass fraction satisfies the transport equations (18) and (19), it follows that all these mixture properties also satisfy these equations. A well-known example is to use $\chi = 1/(\gamma-1)$ as the advected variable (e.g., [1]), i.e.,

$$\frac{\partial}{\partial t}\left(\frac{1}{\gamma-1}\right) + u_j\frac{\partial}{\partial x_j}\left(\frac{1}{\gamma-1}\right) = 0\,. \tag{21}$$

This is exact for perfect gases, by the above argument. This can be seen by

$$\frac{1}{(\gamma_\alpha-1)} = \frac{c_{v,\alpha}}{(c_{p,\alpha}-c_{v,\alpha})} = \frac{c_{v,\alpha}}{R_\alpha}, \tag{22}$$

multiplying by ϕ_α and using the relation (20) yields,

$$\sum_\alpha \phi_\alpha \frac{c_{v,\alpha}}{R_\alpha} = \sum_\alpha \frac{Y_\alpha c_{v,\alpha}}{R}. \tag{23}$$

From equation (12), one obtains

$$\sum_\alpha \frac{Y_\alpha c_{v,\alpha}}{R} = \frac{c_v}{R} = \frac{1}{(\gamma-1)}, \tag{24}$$

hence,

$$\frac{\partial}{\partial t}\left(\frac{1}{\gamma-1}\right) + \mathbf{u}.\nabla\left(\frac{1}{\gamma-1}\right) = \frac{1}{R}\sum_\alpha c_{v,\alpha}\left(\frac{\partial Y_\alpha}{\partial t} + \mathbf{u}.\nabla Y_\alpha\right) = 0. \tag{25}$$

Although not pursued here further, this description can be generalized to imperfect gases by taking into account a source term equal to $1/R\sum_\alpha Y_\alpha \frac{Dc_{v,\alpha}}{Dt} \sim \frac{DT}{Dt}$.

The choice of the advected quantity is very important, as will be shown in Section 4.1.2, since the advection of other quantities can lead to high numerical errors. For instance, the mass fraction advection is suitable for general cases considering perfect and imperfect gases but it may lead to spurious oscillations. The conservative form of the equation (21) also provides numerical oscillations at the interface. Therefore, the advection equation (21) of $1/(\gamma-1)$ is chosen. It remains to determine the volume and mass fractions. Relations (23) and (24) allow to relate the volume fraction to the quantity $1/(\gamma-1)$ which is known from equation (21),

$$\frac{1}{(\gamma-1)} = \sum_\alpha \frac{\phi_\alpha}{(\gamma_\alpha-1)}. \tag{26}$$

Then, using equations (10) and (20) enables the determination of the mass fractions of fluids 1 and 2 from the volume fractions

$$Y_1 = \frac{\phi_1 M_1}{M_2 - \phi_1 (M_2 - M_1)} \tag{27}$$

and $Y_2 = 1 - Y_1$.

3. Numerical methodology

High-order explicit finite-difference schemes are used to solve the governing equations. They have been designed to provide low dissipation and dispersion errors for aeroacoustic computations [8,9]. Some of these methods are adapted for the simulation of multi-component flows.

3.1. Spatial discretization

The spatial derivatives are estimated using the eleven-point fourth-order centred finite difference scheme developed by Bogey and Bailly [8]. The spatial derivative of a variable at point x_0, in the i-direction is approximated by

$$\frac{\partial L}{\partial x_i}(x_0) = \frac{1}{\Delta x} \sum_{j=-5}^{5} a_j L(x_0 + j\Delta x) \,, \tag{28}$$

where Δx is the grid spacing, considered as uniform in the present study, although extensions to non-uniform grids are possible, as in prior work on single-phase flows. The scheme is centred, and its coefficients are chosen such as $a_j = -a_{-j}$, providing no dissipation.

3.2. Spatial selective filtering

Using centred finite differences could result in grid-to-grid oscillations leading to numerical instability. A spatial selective filter is used herein to remove these numerical oscillations [8]. Specifically, an eleven-point sixth-order centred filter is applied at each time step to the variables $U = (\rho, \rho u_k, E, 1/(\gamma - 1))$, yielding at node i:

$$U_i^{sf} = U_i - \sigma^{sf} D_i^{sf} \quad \text{with} \quad D_i^{sf} = \sum_{j=-5}^{5} d_j U_{i+j} \,.$$

This filtering procedure is conservative since the filtering intensity σ^{sf} is constant [40]. In the present study, it is set to $\sigma^{sf} = 1$ in order to completely remove grid-to-grid oscillations. The coefficients d_j are such that $d_j = d_{-j}$, providing no dispersion. The filter has been designed to not significantly affect the waves discretized by more than four mesh points per wavelength [8].

3.3. Temporal advancement

For the temporal advancement, an explicit second-order six-step Runge–Kutta algorithm [8] is employed. It has also been developed in order to minimize the numerical dissipation and dispersion errors, over a wide range of frequencies. The temporal advancement of the variables U from time level n to time level $n+1$, at a time step Δt, is performed in six steps as:

$$U^{n+1} = U^n + \sum_{j=1}^{6} b_j \Delta t^j \frac{\partial^j U^n}{\partial t^j} \,,$$

where b_j are the coefficients of the algorithm [8].

3.4. Discontinuity-capturing methodology

In compressible multi-component flows, various discontinuities arise, including shock waves and interfaces. In the present work, a methodology is proposed to capture these discontinuities without generating significant Gibbs' oscillations. It is based on the use of a spatial filter with a magnitude evaluated from the flow variables. It has been designed by Bogey et al. [9] for single-phase turbulent compressible flows, and is modified herein to also capture deformable interfaces.

3.4.1. Discontinuity spatial filtering

A second-order spatial filter is applied to damp high-frequency oscillations that may appear around discontinuities. The magnitude of this filter is adjusted dynamically from the flow variables in order to be negligible in the absence of oscillations. This filtering is applied at each time step to the variable U, yielding at node i:

$$U_i^{df} = U_i - \left(\sigma_{i+\frac{1}{2}}^{df} D_{i+\frac{1}{2}}^{df} - \sigma_{i-\frac{1}{2}}^{df} D_{i-\frac{1}{2}}^{df} \right) ,$$

$$\text{with} \quad D_{i+\frac{1}{2}}^{df} = \sum_{j=1-n}^{n} c_j U_{i+j} \quad \text{and} \quad D_{i-\frac{1}{2}}^{df} = \sum_{j=1-n}^{n} c_j U_{i+j-1} ,$$

where $c_j = -c_{1-j}$ are the coefficients of the standard second-order filter with $c_1 = -1/4$ and $c_2 = 0$. The magnitude of the filter $0 \leq \sigma^{df} \leq 1$ must be high around discontinuities and negligible otherwise. In order to detect the presence of discontinuities, two sensors r_ρ and r_p are evaluated from density and pressure, respectively. The values of the sensor r_ρ are high in the presence of an interface, a contact discontinuity or a shock wave. Those of the pressure-based sensor r_p are significant for rarefaction waves and shock waves. Since the two sensors are calculated in the same way, only the calculation of the density-based sensor r_ρ is detailed here. First, the high-frequency components are extracted from the density signal, yielding at node i:

$$D\rho_i = \frac{1}{4} \left(-\rho_{i+1} + 2\rho_i - \rho_{i-1} \right) .$$

The magnitude of these components is

$$D\rho_i^{magn} = \frac{1}{4} \left((D\rho_{i+1})^2 + 2(D\rho_i)^2 + (D\rho_{i-1})^2 \right) .$$

Then, the shock sensor r_ρ is defined

$$r_\rho = \frac{D\rho_i^{magn}}{{\rho_i}^2} .$$

Once the sensor r_ρ is known, the spatial filtering intensity σ_ρ^{df} is then determined. It is defined such as to be approximately equal to 1 when oscillations are detected around discontinuities, in other words when the shock sensor r_ρ is high, and the filtering strength σ_ρ^{df} tends to zero in the absence of oscillations, when r_ρ is low. At node i, the intensity σ_ρ^{df} is calculated using the following equation:

$$\sigma_{\rho_i}^{df} = \frac{M_{\rho_i}}{2} \left(1 - \frac{r_{th}}{r_{\rho_i} + \epsilon} + \left| 1 - \frac{r_{th}}{r_{\rho_i} + \epsilon} \right| \right) , \tag{29}$$

where $\epsilon = 10^{-16}$ is introduced to avoid numerical divergence. In this approach, a threshold parameter r_{th} is used to specify the minimum sensor value for which the spatial filtering is applied. For the calculations of σ_ρ^{df} and σ_p^{df}, the same parameter $r_{th} = 2 \times 10^{-5}$ is employed. The intensity σ_ρ^{df}, for instance, is zero when $r_\rho \leq r_{th}$ and σ_ρ^{df} is positive when $r_\rho > r_{th}$. The arbitrary value of the threshold parameter provides appropriate results for the different tests solved. This point is discussed later in Section 4.1.3.

The prefactor M_ρ, the monotony indicator, is introduced to impose $\sigma_\rho^{df} = 0$ in the absence of numerical oscillations. It is estimated from a study of the density monotony around the node i detailed in the next subsection; by design, M_ρ takes values between 0 and 1. Similarly, a monotony indicator M_p is also estimated from pressure.

Finally, the filtering intensity is defined as the maximum of the two intensities estimated from the density and pressure, $\sigma^{df} = \max(\sigma_\rho^{df}, \sigma_p^{df})$. For use in the present conservative formulation, σ^{df} between nodes is obtained from

$$\sigma_{i+\frac{1}{2}}^{df} = \frac{1}{2} \left(\sigma_{i+1}^{df} + \sigma_i^{df} \right) \quad \text{and} \quad \sigma_{i-\frac{1}{2}}^{df} = \frac{1}{2} \left(\sigma_i^{df} + \sigma_{i-1}^{df} \right) .$$

3.4.2. Monotony indicator

The monotony indicator M_ρ in equation (29) is used to avoid damping in the absence of oscillations. Indeed, the shock sensor r_ρ is defined as the ratio between the high-frequency components and the local density. Thus, if the gradient is significant while the local density is weak, the sensor may be higher than the threshold r_{th} even if there is no oscillation. In order to correct this, the indicator M_ρ is introduced in the computation of the filtering magnitude σ_ρ^{df}. It is estimated from the density monotony; likewise, the indicator M_p is estimated from pressure monotony. Since they are computed in exactly the same way, only the calculation of M_ρ is presented below: the density monotony is evaluated using a three-point stencil

$S = \{i-1, i, i+1\}$. First, two variables D^L and D^R, respectively the density variations at the left-hand side and right-hand side of the node i, are considered:

$$D_i^L = \rho_i - \rho_{i-1} \qquad \text{and} \qquad D_i^R = \rho_{i+1} - \rho_i \, .$$

The product of these variables verifies:

$$\begin{cases} D_i^L D_i^R < 0 & \text{if } \rho \text{ has an extremum at node } i \, , \\ D_i^L D_i^R \geq 0 & \text{if } \rho \text{ is monotonous over } S. \end{cases}$$

The variable α is given, at node i, by:

$$\alpha_i = |D_i^R D_i^L| - D_i^R D_i^L \, .$$

Thus, one obtains

$$\begin{cases} \alpha_i > 0 & \text{if } \rho \text{ has an extremum at node } i \, , \\ \alpha_i = 0 & \text{if } \rho \text{ is monotonous over } S. \end{cases}$$

The dispersion error of the discontinuity filtering is directly related to the spatial variations of σ^{df} [9]. Therefore, in order to reduce the dispersion errors due to the filtering, the parameter α is averaged over five mesh points yielding, at node i,

$$\bar{\alpha}_i = \frac{1}{5} \sum_{j=-2}^{2} \alpha_{i+j}$$

Finally, the monotony indicator is defined, at node i, as

$$M_{\rho_i} = \frac{\bar{\alpha}_i}{\bar{\alpha}_i + {\rho_i}^2 \, \epsilon} \, , \tag{30}$$

where $\epsilon = 10^{-16}$ is introduced to avoid numerical divergence. By construction M_{ρ_i} takes values between 0 and 1, and verifies

$$\begin{cases} M_{\rho_i} = 0 & \text{if } \rho \text{ is monotonous over } S \, , \\ M_{\rho_i} \simeq 1 & \text{otherwise.} \end{cases}$$

In this way, the magnitude of the spatial filtering σ_ρ^{df} is set to zero when the solution does not oscillate, but the magnitude is unchanged otherwise.

The present computational approach has been used previously to simulate various viscous and conductive problems for a single fluid, the present work being the generalization to multi-component systems, which is not trivial and includes the introduction of the new monotony indicator. Prior applications in single fluids include the propagation of infra-sounds within homogeneous and inhomogeneous media [46], and turbulent channel flows [41]. Several simulations of turbulent jets have also been performed, notably, subsonic jets at different Reynolds number [11], an overexpanded jet at a Mach number of 3.3 [18] and supersonic round jets impinging on a flat plate [10].

4. 1D test cases

In order to validate the present algorithm, several one-dimensional test cases are considered here. In these, equations (2) and advection equation (21), supplemented with the perfect gas equation of state (17) are solved.

4.1. Gas–gas interface advection

The first test case concerns the advection of an interface between two gases at constant pressure and velocity [32]. This configuration often arises in two phase flows, for instance before and after a shock/interface interaction. We first solve this in order to verify that the algorithm is able to capture an interface, and to assess the effects of the monotony indicators on the solutions. Then, the test is considered in order to exhibit the influence of the choice of the advected variables governing the interface. Finally, we use different values for the threshold parameter r_{th}, which allows us to compute the discontinuity filtering magnitude σ_ρ^{df} in equation (29).

At time $t = 0$, the conditions are:

$$(\rho, u, p, \gamma) = \begin{cases} (1, 0.5, 1/1.4, 1.4) & \text{for } x \leq 0 \, , \\ (10, 0.5, 1/1.4, 1.2) & \text{for } x > 0 \, . \end{cases}$$

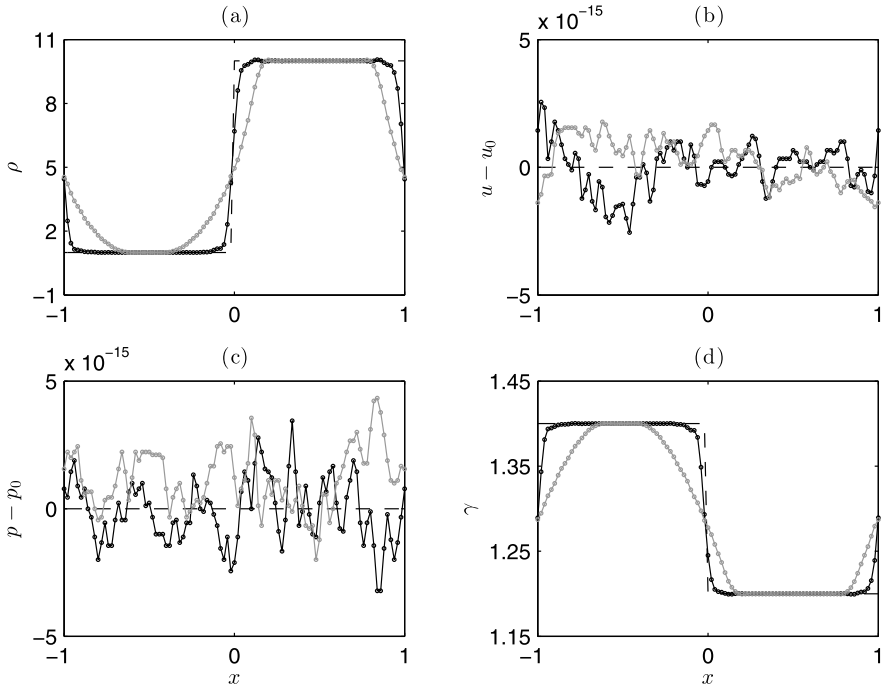

Fig. 1. Gas–gas interface advection. Representation of (a) the density, (b) the difference with respect to the analytical solution for velocity $u - u_0$, (c) the difference with respect to the analytical solution for pressure $p - p_0$ and (d) γ at time $t = 4$. Solutions obtained —— without and —— with monotony indicators; • mesh points, – – – analytical solutions.

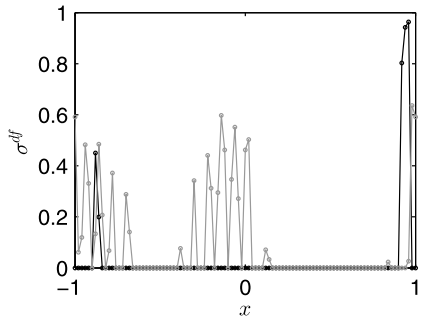

Fig. 2. Gas–gas interface advection. Representation of the intensity of the discontinuity filtering σ^{df} at time $t = 4$. Solutions obtained —— without and —— with monotony indicators; • mesh points.

Only density and γ are discontinuous at the interface whereas pressure and velocity are uniform. The viscosity and the thermal conductivity of both fluids are zero. Their effects on the results are found not significant (we defer discussion of that to the end of Sec. 4.1.2). The problem is computed using a uniform grid spacing $\Delta x = 0.02$ and a time step $\Delta t = 0.016$. At time $t = 0$, the highest non-dimensional speed of sound is equal to $c = \sqrt{\gamma p/\rho} = 1$, leading to $c\Delta t/\Delta x = 0.8$. Periodic boundary conditions are imposed at $x = -1$ and $x = 1$. The solution is computed up to time $t = 4$. At that time, the interface, initially at $x = 0$, returns to its initial position.

4.1.1. Validation of the algorithm

The results obtained at $t = 4$ for density, γ and the differences between the numerical and analytical solutions for velocity and pressure, respectively $u - u_0$ and $p - p_0$, are presented in Fig. 1. The analytical solutions are represented in dashed lines. The numerical results in black and in gray are computed with and without using the monotony indicators, respectively. In the latter case, the density and γ profiles in Figs. 1(a) and 1(d) are strongly asymmetric. In the former case, using the indicators, the gas–gas interface is accurately propagated and discretized by only five mesh points. The velocity and pressure errors in Figs. 1(b) and 1(c) are of the order of 10^{-15} in both cases.

The intensity of the discontinuity filtering σ^{df} at final time is represented in Fig. 2. It is estimated either with or without the monotony indicators. Without the monotony indicators, the filtering intensity is stronger on the left part of the interface than on the right part. Indeed, the local density ρ_i is lower in the left region, leading to a higher sensor

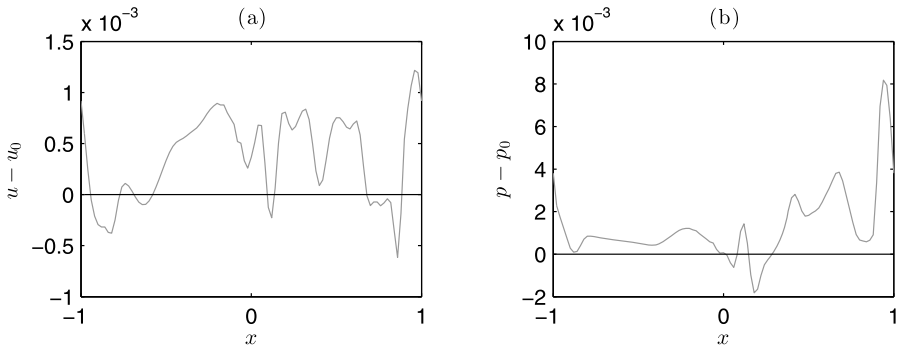

Fig. 3. Representation of the differences between numerical and analytical solutions for (a) velocity $u - u_0$ and (b) pressure $p - p_0$ at time $t = 4$; solutions obtained using the advection equation of — γ and — $1/(\gamma - 1)$.

value r_ρ. Consequently, the solutions are significantly damped, leading to the asymmetry of the profile. Using the monotony indicators, the filtering intensity is not zero only on five mesh points located around $x = -0.8$ and $x = 0.9$. In addition, the filtering intensity is null across the interface. At that time, no significant oscillation is detected across the interface, most likely because they have already been damped by the discontinuity filtering. Thus, thanks to the indicators which set the amplitude of the filtering to zero in the absence of oscillations, the filtering is only applied when Gibbs' oscillations are generated.

In order to verify that the monotony indicators are also effective in the case of a large density ratio, an additional problem has been solved. It consists in the advection of an interface at constant pressure and velocity with an initial density ratio of 10^3. The corresponding results (not shown) indicate that the interface is correctly propagated and the filtering only applies when significant oscillations are generated. Therefore, the monotony indicators enable the simulations of flows containing large density ratios as observed around an air–water interface.

4.1.2. Influence of the advected variables governing the interface

In order to assess the influence of the choice of the advected variable in equation (18), two simulations are performed. In the first case, $\chi = \gamma$ is used and in the second case, $\chi = 1/(\gamma - 1)$ is used.

The differences between numerical and analytical solutions for velocity and pressure are presented in Figs. 3(a) and 3(b), respectively. The results in gray are obtained employing γ and those in black using $1/(\gamma - 1)$. In the first case, the pressure and velocity errors are of the order of 10^{-3} whereas, in the second case, they are of the order of 10^{-15}. Therefore, if the variable γ is advected, pressure oscillations are generated at the interface and propagate. Note that the test case has also been solved using the conservative and the non-conservative forms of the advection equation of the mass fraction, both leading to pressure oscillations of the order of 10^{-2}. We also considered the advection equation of $1/(\gamma - 1)$ in conservative form to solve this problem and other 1-D test cases. This yields oscillating and incorrect results as observed in other studies [1,32,56].

The choice of the advection of $1/(\gamma - 1)$ was justified by Abgrall [1] by considering an inviscid flow containing two gases at same pressure and velocity. Since pressure and velocity are uniform, the total energy conservation equation of system (2) can be expressed as:

$$\frac{\partial E}{\partial t} + u\frac{\partial E}{\partial x} = 0. \tag{31}$$

Substituting the total energy E using the perfect gas equation of state (17), the previous equation becomes

$$\frac{\partial}{\partial t}\left(\frac{p}{\gamma - 1}\right) + u\frac{\partial}{\partial x}\left(\frac{p}{\gamma - 1}\right) = 0,$$

yielding equation (21), the advection equation for $1/(\gamma - 1)$. Therefore, the advection of $1/(\gamma - 1)$ is chosen in order to propagate a deformable interface between perfect gases.

The derivation of the equation (21) from equation (31) is also valid for a viscous and conductive flow containing two fluids at the same pressure, velocity and temperature, as the viscous and conductive terms then vanish. In order to validate the algorithm in the case of a viscous flow, an additional test case has been solved using the Navier–Stokes equations including viscosity and thermal conductivity of both fluids. It involves the advection of a helium–air interface at constant pressure, velocity and temperature. The results are very similar to those obtained using Euler's equations (not shown).

4.1.3. Influence of the threshold parameter r_{th}

The influence of the threshold parameter r_{th} is now investigated by solving the test case using $r_{th} = 2 \times 10^{-6}$, 2×10^{-5} and 2×10^{-4}. The threshold parameter provides the minimum value of sensors r_ρ and r_p, from which the discontinuity filtering applies. This parameter can be adjusted according to the flow that is considered.

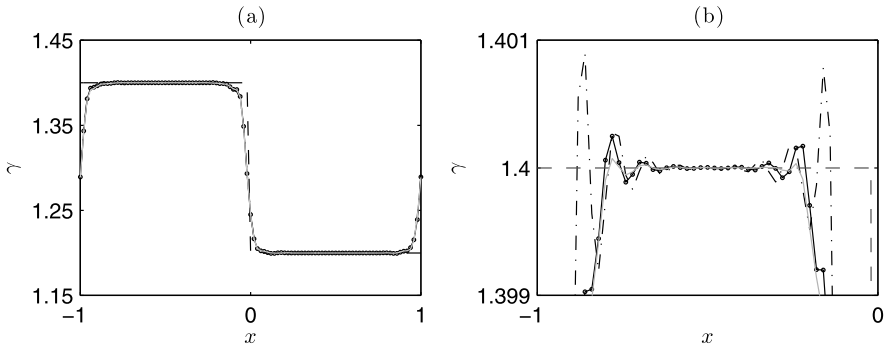

Fig. 4. Representation of the γ profile (a) in the entire domain and (b) between $x=-1$ and $x=0$ at $t=4$; numerical solutions obtained using the threshold values —— 2×10^{-6}, —●— 2×10^{-5} and -·—·- 2×10^{-4}; - - - analytical solution.

The profile of γ obtained at $t=4$ is presented between $x=-1$ and $x=1$ in Fig. 4(a) and between -1 and 0 in Fig. 4(b). The solutions obtained for $r_{th}=2\times10^{-4}$, 2×10^{-5} and 2×10^{-6} are presented in dash–dot, in black and in gray, respectively. Very weak oscillations are observed using the lowest threshold, whereas significant Gibbs' oscillations appear around the interface using the highest threshold. A numerical solution with a sharp discontinuity and weak oscillations is obtained using the intermediate value $r_{th}=2\times10^{-5}$. Therefore, this value is used in what follows.

4.2. Inviscid gas–gas shock-tube

This test case concerns a shock-tube containing two inviscid gases [2]. The interest here is to simulate both a shock wave and an interface within the same flow. The conditions at $t=0$ are:

$$(\rho,u,p,\gamma)=\begin{cases}(1,0,500,1.4), & \text{if } x\leq 0.5\,,\\ (1,0,0.2,1.6), & \text{if } x>0.5\,.\end{cases}$$

The density and the velocity are uniform. The discontinuities in the pressure and γ profiles result in the formation of a shock wave and an interface. The computational domain is composed of 800 cells from $x=0$ to $x=1$. The solutions are calculated up to time $t=0.01$ using a time step $\Delta t=5\times10^{-5}$, yielding a Courant–Friedrich–Lewy number $CFL=c\Delta t/\Delta x=1.06$ where $c=\sqrt{\gamma p/\rho}=26.5$ is the maximum non-dimensional speed of sound of the flow at $t=0$.

The numerical and analytical results obtained at $t=0.01$ for density, velocity, pressure and γ are shown in Fig. 5. The numerical and the analytical results are in black and in gray dashes, respectively. Two discontinuities appear in the density profile in Fig. 5(a): an interface and a shock wave, indicated by the letters I and S, respectively. The interface observed at $x=0.64$, and the shock wave at $x=0.7$ travel in the downstream direction. Also, a rarefaction wave propagating in the upstream direction is observed in the density profile between $x=0.21$ and $x=0.39$, indicated by the letter R. The velocity and the pressure profiles in Figs. 5(b) and 5(c) only show the rarefaction wave and the shock wave. The maximum velocity is located between these two waves reaching $u=13.25$. Finally, only the interface is visible in the γ profile in Fig. 5(d). Indeed, the heat capacity ratio is constant in each fluid and discontinuous at the interface. Initially, the shock wave and the interface are both located at $x=0.5$. At the final time, the interface is upstream of the shock wave. Therefore, the interface is advected at a lower speed than the shock wave. This is due to the fact that the speed behind a shock is smaller than the shock speed.

The numerical results are in very good agreement with the analytical solutions and no significant oscillations are found around the discontinuities. All the singularities are accurately propagated and the shock wave is discretized by only five mesh points. However, the density discontinuity is slightly damped on the right-hand side of the interface because of the interaction of the shock wave with the interface at the very beginning of the simulation.

In Fig. 6, the intensities of the discontinuity filtering σ_p^{df} and σ_ρ^{df} obtained at $t=0.01$ are presented. Both intensities are null everywhere except around the shock wave, including around the rarefaction wave and the interface. The intensity σ_p^{df} estimated from the pressure is approximately equal to one over twelve mesh points from $x=0.67$ to $x=0.69$. The intensity σ_ρ^{df} is not null from $x=0.67$ to $x=0.68$. This indicates that some oscillations remain around the shock wave on the density and the pressure. In addition, since the intensity of the discontinuity filtering σ^{df} is given by the maximum of σ_p^{df} and σ_ρ^{df}, σ^{df} is identical to σ_p^{df} at this time.

In Fig. 7, the density obtained at $t=0.01$ using five meshes containing 800, 5×10^3, 10^4, 5×10^4 and 10^5 cells are represented. The density profiles are zoomed in around the interface, and are compared with the analytical solution. The numerical solutions are in agreement with the analytical one, indicating that the interface is accurately propagated for all grids. A sharper interface is obtained using a finer mesh, as awaited. In order to assess the convergence of the results, the

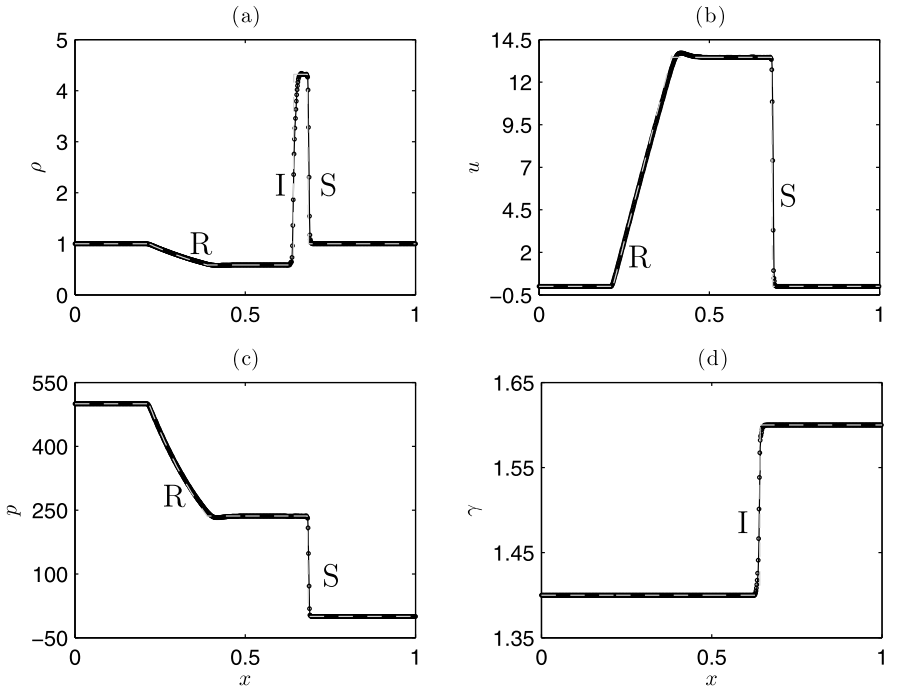

Fig. 5. Inviscid gas–gas shock-tube. Results for (a) density, (b) velocity, (c) pressure and (d) γ at $t = 0.01$; —— numerical and - - - analytical solutions, • mesh points; the letters R, I and S indicate the rarefaction wave, the interface and the shock wave, respectively.

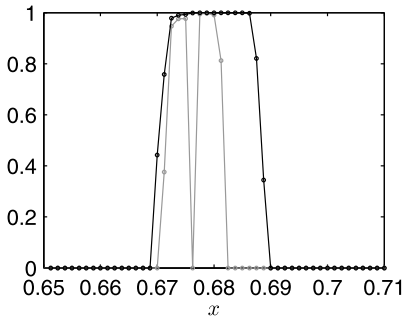

Fig. 6. Inviscid gas–gas shock-tube. Solutions at $t = 0.01$ for the intensities of the discontinuity filtering —— $\sigma_\rho{}^{df}$ and —— σ_p^{df}; • mesh points.

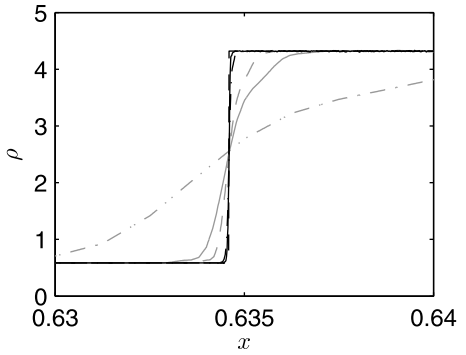

Fig. 7. Inviscid gas–gas shock-tube. Results for the density zoomed in around the interface and computed at $t = 0.01$ on meshes containing - · — · 800, —— 5×10^3, - - - 10^4, - · — · 5×10^4 and —— 10^5 cells; - - - analytical solution.

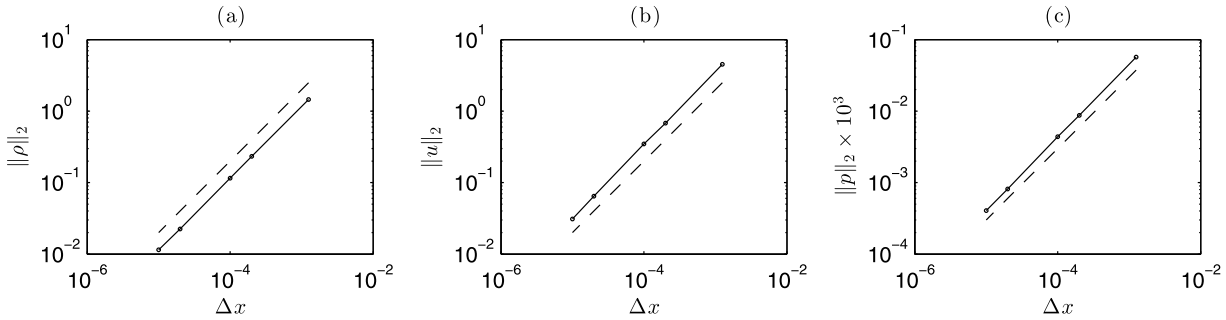

Fig. 8. Inviscid gas–gas shock-tube. Norm of the error on (a) the density, (b) the velocity and (c) the pressure as a function of Δx, the dash line indicates a variation proportional to Δx.

norm of the errors is calculated for density, pressure and velocity, and shown in Fig. 8 as a function of mesh spacing Δx. It is defined, at node i, by

$$\|L\|_2 = \sqrt{\frac{1}{n_x}\sum_i (L_{e,i} - L_{n,i})^2},$$

where L_e and L_n are the exact and numerical solutions, respectively, and n_x is the number of mesh points. As expected, the error decreases when the grid is refined. Unlike the results of Gallouët et al. [20], the same convergence rate is found for the three variables. More precisely, as indicated by the line represented in black dashes and also by the computation of the convergence rate, the error is proportional to Δx. This is consistent with the order of the dispersion error of the discontinuity capturing filtering [9].

4.3. Viscous helium–air shock-tube

The test case concerns a shock-tube containing helium in the left half of the domain and air in the right half of the domain [1]. It is solved using either the Euler equations or the Navier–Stokes equations. In the second case, the viscosity and the thermal conductivity of both fluids are estimated using empirical relations given in Appendix A. The conditions at $t = 0$ are:

$$(\rho, u, p, \gamma) = \begin{cases} (14.54903\ \text{kg.m}^{-3}, 0, 194.3 \times 10^5\ \text{Pa}, 1.67), & \text{if } x \leq 0.5\ \text{m} \\ (1.16355\ \text{kg.m}^{-3}, 0, 1 \times 10^5\ \text{Pa}, 1.4), & \text{if } x > 0.5\ \text{m} \end{cases}$$

Initially, the velocity is zero everywhere. The shock wave and the helium–air interface are superimposed at the centre of the domain. The computational domain is discretized into 800 cells, and ranges from $x = 0$ to $x = 1$ m. The solutions are calculated up to $t = 2 \times 10^{-4}$ s using a CFL number $c_{he}\Delta t/\Delta x = 0.8$, where the speed of sound in helium is equal to $c_{he} = \sqrt{\gamma p/\rho} = 1493.4\ \text{m.s}^{-1}$, which is the maximum speed of sound of the flow at $t = 0$.

The results obtained at final time for density, velocity, pressure, and γ are presented in Fig. 9. The solutions obtained using the Euler equations and the Navier–Stokes equations are depicted in gray and black, respectively. The analytical solutions for the inviscid flow are given by black dashed lines. Three singularities appear on the density profile in Fig. 9(a): a rarefaction wave between $x = 0.2$ m and $x = 0.58$ m, an interface at $x = 0.78$ m and a shock wave at $x = 0.85$ m. The velocity and the pressure profiles, in Figs. 9(b) and 9(c), only show two singularities which are the rarefaction wave and the shock wave. Finally, on the profile of γ in Fig. 9(d), only the interface is observed. For both viscous and inviscid flows, a peak is observed on velocity and pressure immediately upstream of the rarefaction wave, and also on the density profile downstream of the interface. Small oscillations remain on the γ profile downstream of the interface. However, using both Euler and Navier–Stokes equations, all the discontinuities are propagated accurately, and remain sharp.

5. 2D simulations

Two flows that have been studied experimentally previously, involving a plane shock wave and an interface between two perfect gases, are considered in this section. They are simulated by solving the two-dimensional Navier–Stokes equations (2) combined with the equations governing the interface advection (21) and the perfect gas equation of state (17).

5.1. Richtmyer–Meshkov instability

5.1.1. Initial configuration

The first problem is Richtmyer–Meshkov instability (RMI) developing at the interface between two gases. The instability is formed after the passage of a shock wave through a perturbed interface between two fluids with different densities [13].

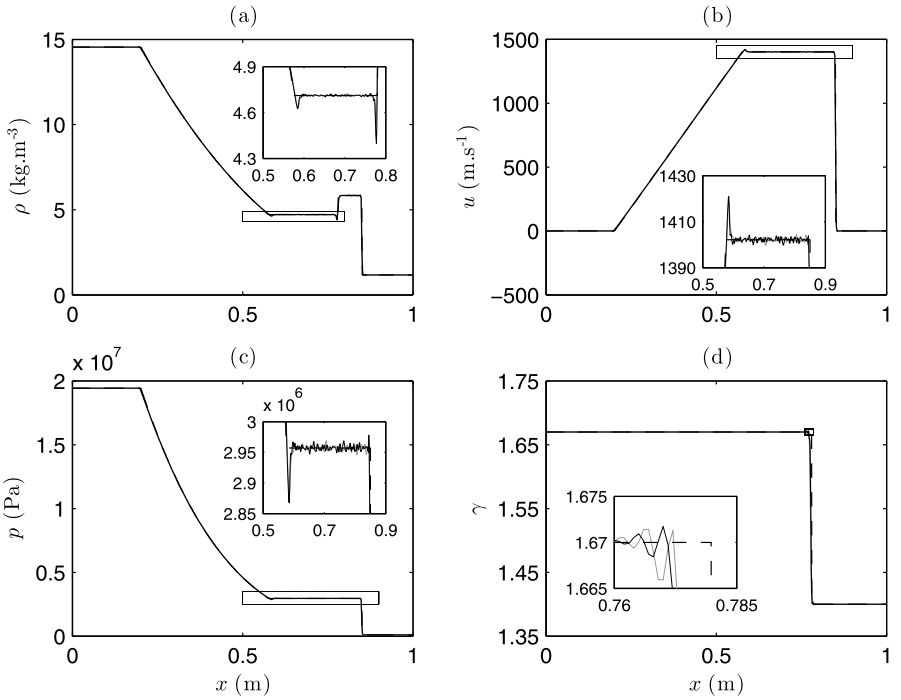

Fig. 9. Viscous helium–air shock-tube. Results for (a) density, (b) velocity, (c) pressure and (d) γ at $t = 2 \times 10^{-4}$ s; solutions obtained using the —— Euler and the —— Navier–Stokes equations; - - - analytical solutions. The black squares indicate the zones where the solutions are zoomed in.

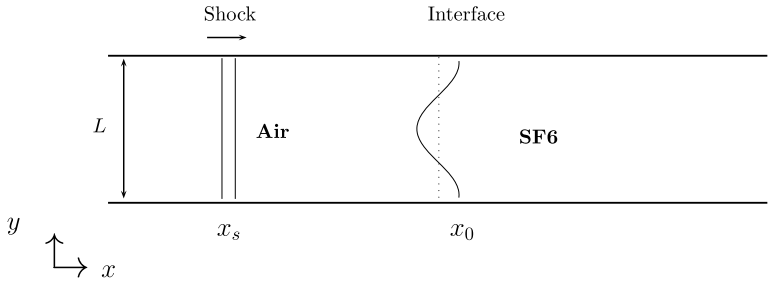

Fig. 10. Initial configuration for the study of Richtmyer–Meshkov instability [30].

In the present work, the RMI grows between air and sulphur hexafluoride (SF6), as in the experiments of Jacobs and Krivets [30], that were performed in a vertical shock tube at ambient temperature and pressure. The shock tube of square cross section, was shaken horizontally in order to create a sinusoidal interface without the use of a solid membrane. Then, a plane shock wave was generated in the air and impacted the perturbed interface.

The initial configuration, corresponding to the experimental set up [30], is drawn in Fig. 10. A shock wave with a Mach number of $M = 1.29$ is generated in air at $x = x_s$. The air–SF6 interface is initially located at x_0 and the distance between x_s and x_0 is equal to 2 cm. The interface is perturbed using a cosine profile [27,61]. Thus, its initial position x_{int} is expressed as:

$$x_{int} = x_0 + a \times \cos\left(\frac{2\pi}{\lambda} y\right),$$

where $a = 2.9$ mm is the perturbation amplitude and $\lambda = 59$ mm is the cosine wavelength. Experimentally, the distance between the two walls of the shock tube is larger than the perturbation wavelength λ. Consequently, multiple instabilities develop on the interface. In the simulation, the upper and lower boundaries of the domain are spaced by the distance $L = \lambda$, and periodic conditions are imposed on these two boundaries. Therefore, only one wavelength is simulated. Radiation conditions are imposed at the upstream and downstream boundaries [60]. The initial conditions for density, axial velocity, pressure and γ are:

Table 1
Number of grid cells n_x and n_y contained in the meshes *ny64*, *ny128*, *ny256* and *ny512* in the x and y directions.

	n_x	n_y	Number of cells
ny64	1023	64	65×10^3
ny128	2046	128	262×10^3
ny256	4092	256	1×10^6
ny512	8186	512	4.2×10^6

$$(\rho, u_x, p, \gamma) = \begin{cases} (2.2997\ \text{kg.m}^{-3}, 136\ \text{m.s}^{-1}, 179750\ \text{Pa}, 1.27) & \text{for } x \leq x_s \\ (1.4933\ \text{kg.m}^{-3}, 0, 101325\ \text{Pa}, 1.27) & \text{for } x_s < x \leq x_{int} \\ (6.0156\ \text{kg.m}^{-3}, 0, 101325\ \text{Pa}, 1.0984) & \text{for } x > x_{int} \end{cases}$$

The air density of 1.4933 kg.m^{-3} is higher than the density provided by the ideal gas law at temperature $T = 296$ K and pressure $p = 101325$ Pa yielding $\rho = 1.194$ kg.m^{-3}. Indeed, in the experiments the air was mixed with 25% of gaseous acetone in order to allow the flow to be visualized when lighted up by a laser sheet. Therefore, the molar mass of the air–acetone mixture M_{aa} is estimated from:

$$M_{aa} = 0.25 M_{acetone} + 0.75 M_{air} = 36.27\ \text{g.mol}^{-1},$$

where the molar mass of air $M_{air} \simeq 29$ g.mol^{-1} and the molar mass of acetone $M_{acetone} = 58.08$ g.mol^{-1}. The heat capacity ratio of the air–acetone mixture $\gamma_{aa} = 1.27$ and the temperature of the experiment have been communicated by Jacobs and Krivets [31]. The densities of the air–acetone mixture ρ_{aa} and of the SF6 ρ_{SF6} ahead of the shock are obtained using the ideal gas law, such as:

$$\rho_{aa} = \frac{p}{T}\frac{M_{aa}}{R_u} = 1.4933\ \text{kg.m}^{-3} \ \text{ and } \ \rho_{SF6} = \frac{p}{T}\frac{M_{SF6}}{R_u} = 6.0156\ \text{kg.m}^{-3},$$

where $M_{SF6} = 146.06$ g.mol^{-1} is the molar mass of SF6 and $R_u = 3.14462$ J.mol^{-1}.K^{-1} is the universal gas constant. The Atwood number is then given by

$$A = \frac{\rho_{SF6} - \rho_{aa}}{\rho_{SF6} + \rho_{aa}} = 0.6023.$$

In the experiments [30], this is approximately equal to 0.6. Finally, the conditions behind the initial plane shock wave were computed from the normal shock relations [5].

In the experiments [30], the initial thickness of the interface between air and SF6 is about 5 mm. This thickness is due to mass diffusion between the two gases. In the simulation, the interface is initially specified by a hyperbolic tangent profile centred on the interface position x_{int} [61]. The thickness $\delta_{99}^{int} = 5$ mm is defined as the distance between the positions where the volume fraction is equal to 0.01 and 0.99. Therefore, the volume fractions of the air–acetone mixture ϕ_{aa} and of the SF6 ϕ_{SF6} are initially provided by:

$$\begin{cases} \phi_{aa} = \dfrac{1}{2}\left[1 - \tanh\left(\dfrac{x - x_{int}}{\delta_{th}}\right)\right], \\ \phi_{SF6} = 1 - \phi_{aa}\ , \end{cases} \tag{32}$$

where δ_{th} is equal to:

$$\delta_{th} = \delta_{99}^{int} \Big/ \left(-2\tanh^{-1}\left(\frac{0.01 - 0.5}{0.5}\right)\right).$$

Four uniform grids, containing 64, 128, 256 and 512 mesh cells in the y-direction, and denoted by *ny64*, *ny128*, *ny256* and *ny512*, respectively, are used. The number of cells in the x-direction and y-direction, are given in Table 1. The time step Δt is defined by the $CFL = c_{aa}\frac{\Delta t}{\Delta x} = 0.5$ where $c_{aa} = 293.5$ m.s^{-1} is the speed of sound in the air–acetone mixture. In order to consider the same shock using the four grids, the shock is initially defined by imposing the hyperbolic tangent profile of equation (32) on density, axial velocity and pressure. The shock thickness is arbitrary set to $\delta_{99}^{sh} = 3.7$ mm in order to discretize the shock wave by 4 mesh cells on the coarsest grid *ny64*, and consequently by $8\Delta x$, $16\Delta x$ and $32\Delta x$ using the grids *ny128*, *ny256* and *ny512*, respectively.

5.1.2. Results

The density fields obtained at $t = 1.76$, 3.06, 4.96 and 5.86 ms using grids *ny128*, *ny256* and *ny512* are compared with the experimental visualisations of Jacobs and Krivets [30] in Fig. 11. The time $t = 0$ corresponds to the moment when there is the first contact between the shock and the interface. The SF6 density is in black and the density of the air–acetone

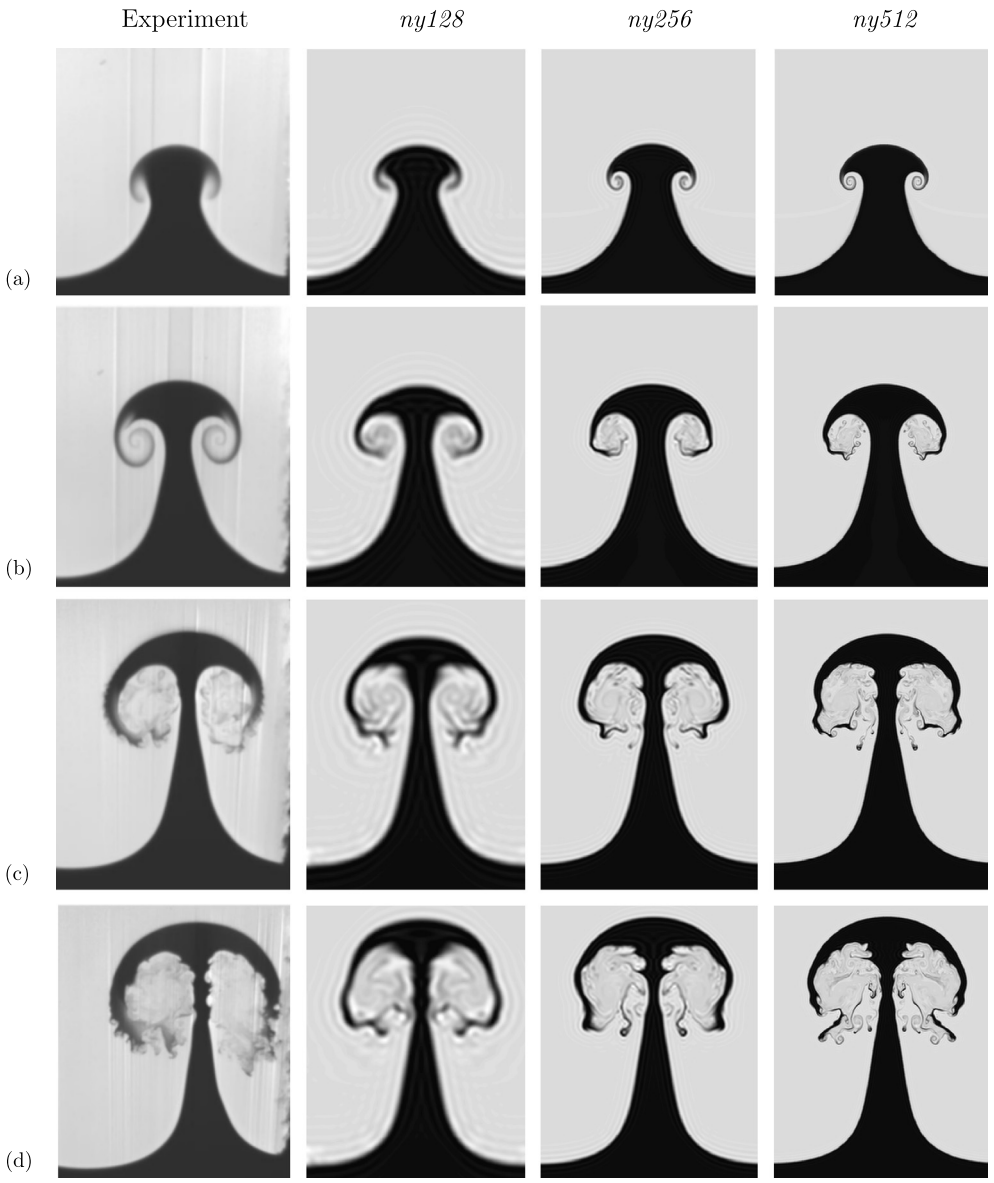

Fig. 11. Experimental visualisations of Jacobs and Krivets [30] (first column) at (a) $t = 1.76$ ms, (b) $t = 3.06$ ms, (c) $t = 4.96$ ms and (d) $t = 5.86$ ms; and density fields obtained using the meshes *ny128* (second column), *ny256* (third column) and *ny512* (fourth column). The air–acetone mixture is in gray and the SF6 in black.

mixture is in gray. For the comparisons, the density fields are rotated 90° clockwise. Note that the discontinuity-capturing methodology is not used here for two reasons. Firstly, it is not necessary because the shock is weak and the interface is thick. Secondly, slight instabilities are generated on the interface when the methodology is employed in this case. Similar instabilities have been observed in other computations from the literature [42,61], but their origin is unclear.

At time $t = 1.76$ ms in Fig. 11(a), the RMI begins to develop. The air–acetone mixture is accelerated more rapidly than the SF6, leading to the formation of a spike of SF6 penetrating the air–acetone mixture. On the left- and right-hand side of the spike spirals of SF6 are formed in the simulations using *ny256* and *ny512*. At the second time, in Fig. 11(b), the instability grows into a mushroom shape. Two spirals are visible in the experiment on the left- and right-hand side of the mushroom. In the simulations, they are disrupted leading to smaller structures which are better defined using the finest mesh. In Figs. 11(c) and 11(d), the two fluids are mixed at each side of the mushroom stem and small perturbations appear on the stem. The simulation performed on the finest mesh allows us to better distinguish the small structures and provides instability shapes which are similar to those obtained experimentally.

As depicted in Fig. 12, the amplitude a of the RMI is defined by half the distance $x_t - x_b$ between the mushroom's summit and its base. The width of the stem w_s is measured at $x = (x_b + x_t)/2$. The width of the mushroom's head w_h is given by the maximum width of the instability between x_t and $x = x_t - 0.75a$. The temporal variations of the RMI amplitude are

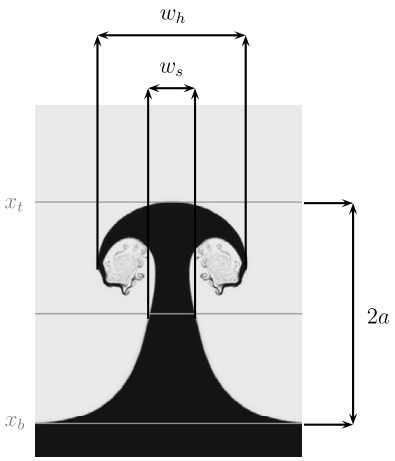

Fig. 12. Representation of the RMI amplitude a, the width of the mushroom's stem w_s and the width of the mushroom's head w_h.

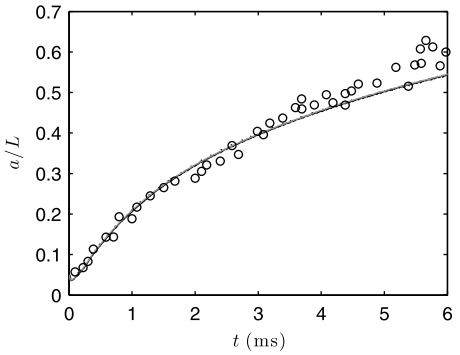

Fig. 13. Temporal variations of the RMI amplitude a normalized by the width of the computational domain L; solutions obtained using the meshes - - - *ny64*, ····· *ny128*, – – – *ny256* and —— *ny512*; ∘ experimental data [30].

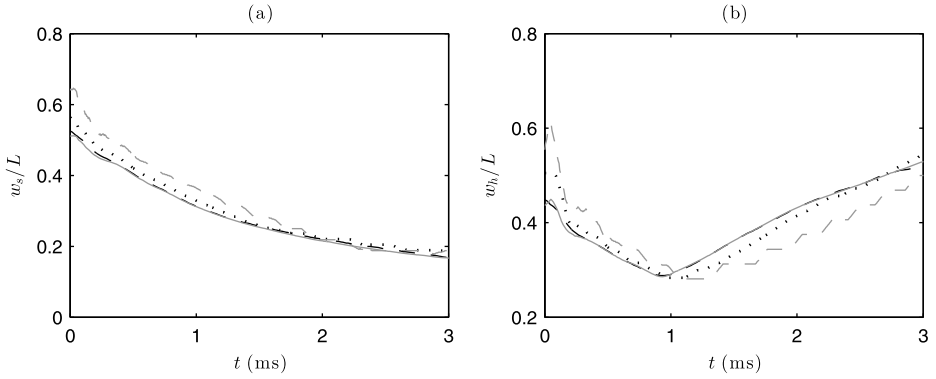

Fig. 14. Temporal variations of the width of (a) the mushroom's stem w_s and of (b) the mushroom's head w_h, normalized by the width of the computational domain L; solutions obtained using the meshes - - - *ny64*, ····· *ny128*, – – – *ny256* and —— *ny512*.

presented in Fig. 13. The results obtained using the four meshes *ny64*, *ny128*, *ny256* and *ny512* are superimposed, indicating that the instability amplitude is not sensitive to the grid refinement. They are also in good agreement with the experimental data in black circles [30]. After $t = 3$ ms, the amplitude is slightly lower in the simulations than in the experiments. This may be due to differences in initial conditions, or in fluid properties. In the experiments for instance, the initial interface perturbation is not perfectly sinusoidal.

The temporal variations of the width of the mushroom's stem are shown in Fig. 14(a). As the instability grows, the width of the stem decreases. The variations of the width of the mushroom's head are also displayed in Fig. 14(b). From $t = 0$ to 1 ms, the width decreases and then increases after $t = 1$ ms. At early times, the sinusoidal interface remains sinusoidal with an increasing amplitude. Therefore, the spike becomes longer and thinner and its width decreases. At later

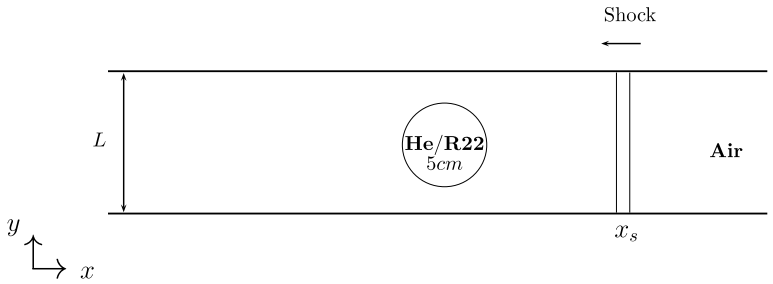

Fig. 15. Initial experimental configuration for the study of a cylindrical helium or R22 bubble, hit by a shock wave at $M = 1.22$ [24].

times, a mushroom head appears which becomes larger in time. Therefore, the width w_h increases. For both widths w_s and w_h, significant differences are observed between the results computed on the grids *ny64*, *ny128* and *ny256*. However, the solutions estimated using *ny256* and *ny512* are very similar. Consequently, the simulation performed using *ny256* appears to be converged with respect to the grid.

5.2. Cylindrical bubble hit by a shock wave

The second two-dimensional problem concerns a shock wave travelling through air, and impacting on a cylindrical bubble of helium or chlorodifluoromethane (R22), studied previously experimentally by Haas and Sturtevant [24]. Similar experiments with spherical bubbles have been conducted by Layes et al. [43]. They have been simulated including viscous effects by Giordano and Burtschell [21]. The experiments of Haas and Sturtevant [24] were performed using a cylindrical bubble. Thus, the 2-D simulation corresponds with this experimental configuration. Two cases leading to strongly different bubble shapes are considered: a shock wave travelling from heavy gas (air) to a light gas (helium bubble), and a shock wave propagating from light gas (air) to heavy gas (R22 bubble).

5.2.1. Initial configuration

The initial configuration depicted in Fig. 15 is considered. The domain width is $L = 8.9$ cm and the bubble of diameter $D = 5$ cm is centred along the y-direction. The shock wave is initially generated in air at the position x_s, and is propagated from right to left with a Mach number $M = 1.22$. The initial conditions for density, axial velocity, pressure and γ are:

$$(\rho, u_x, p, \gamma) = \begin{cases} (1.66\ \text{kg.m}^{-3}, -114\ \text{m.s}^{-1}, 159080.98\ \text{Pa}, 1.4) & \text{for } x > x_s \\ (1.2062\ \text{kg.m}^{-3}, 0, 101325\ \text{Pa}, 1.4) & \text{in air, for } x \leq x_s \\ (0.2204\ \text{kg.m}^{-3}, 0, 101325\ \text{Pa}, 1.6451) & \text{inside the helium bubble} \\ (3.5965\ \text{kg.m}^{-3}, 0, 101325\ \text{Pa}, 1.1847) & \text{inside the R22 bubble} \end{cases}$$

In the experiments, the cylindrical bubble is shaped using a solid membrane. Because of the membrane's permeability, the helium in the bubble is initially mixed with 28% of mass concentration of air. Therefore, the mass fractions of helium and air in the bubble are equal to $Y_h = 0.72$ and $Y_a = 0.28$, respectively. Consequently, the molar mass of this helium–air mixture M_{ha} is (see equation (20))

$$M_{ha} = \left(\frac{0.28}{M_h} + \frac{0.72}{M_{air}} \right)^{-1} = 5.3\ \text{g.mol}^{-1}\,,$$

where the molar mass of air is $M_{air} \simeq 29\ \text{g.mol}^{-1}$ and the molar mass of helium is $M_h = 4.0026\ \text{g.mol}^{-1}$. The heat capacities at constant pressure and volume of the helium–air mixture, $c_{p,ha}$ and $c_{v,ha}$, respectively, are given by

$$\begin{cases} c_{p,ha} = Y_h c_{p,h} + Y_a c_{p,air} = 4026\ \text{J.kg}^{-1}.\text{K}^{-1}\,, \\ c_{v,ha} = Y_h c_{v,h} + Y_a c_{v,air} = 2447.3\ \text{J.kg}^{-1}.\text{K}^{-1}\,, \end{cases}$$

where the heat capacities of helium are $c_{p,h} = 5201\ \text{J.kg}^{-1}.\text{K}^{-1}$ and $c_{v,h} = 3120\ \text{J.kg}^{-1}.\text{K}^{-1}$ and, the heat capacities of air are $c_{p,air} = 1004.5\ \text{J.kg}^{-1}.\text{K}^{-1}$ and $c_{v,air} = 717.5\ \text{J.kg}^{-1}.\text{K}^{-1}$. Thus, the ratio of heat capacity of the helium–air mixture γ_{ha} is

$$\gamma_{ha} = \frac{c_{p,ha}}{c_{v,ha}} = 1.6451\,.$$

The densities ρ_{ha}, ρ_{R22} and ρ_{air} of the helium–air mixture, of the R22 and of the air ahead of the shock, respectively, are provided by the ideal gas law:

Table 2
Number of grid cells n_x and n_y in the x and y directions respectively, contained in the 4 meshes R_0100, R_0200, R_0400 and R_0800.

	n_x	n_y	Number of cells
R_0100	2000	356	712×10^3
R_0200	4000	712	2.85×10^6
R_0400	8000	1424	11.4×10^6
R_0800	16000	2848	23×10^6

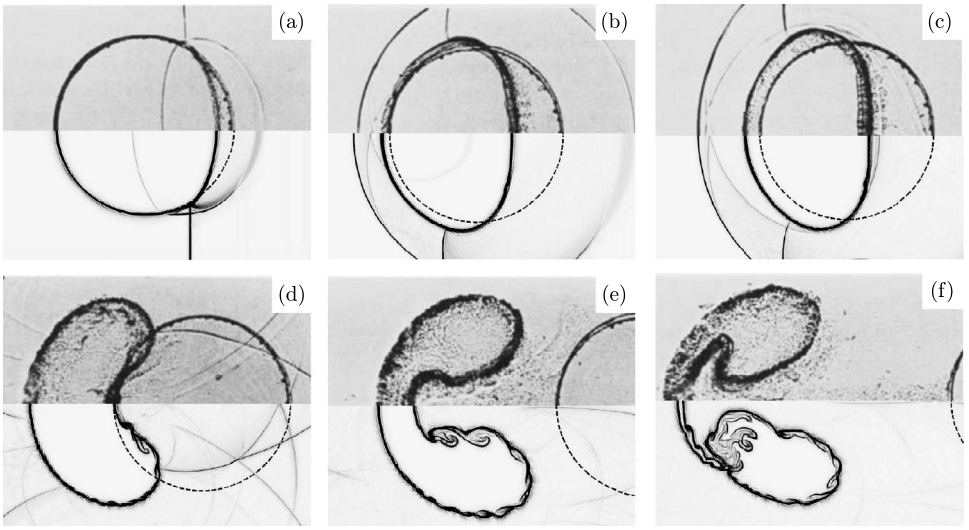

Fig. 16. Helium bubble: numerical Schlieren pictures (lower-half pictures) and experimental shadow-photographs (upper-half pictures) [24] obtained at (a) $t = 32$ µs, (b) $t = 82$ µs, (c) $t = 102$ µs, (d) $t = 245$ µs, (e) $t = 427$ µs and (f) $t = 674$ µs.

$$\begin{cases} \rho_{ha} = \dfrac{p}{T}\dfrac{M_{ha}}{R_u} = 0.2204 \text{ kg.m}^{-3}, \\ \rho_{R22} = \dfrac{p}{T}\dfrac{M_{R22}}{R_u} = 3.5965 \text{ kg.m}^{-3}, \\ \rho_{air} = \dfrac{p}{T}\dfrac{M_{air}}{R_u} = 1.2062 \text{ kg.m}^{-3}, \end{cases}$$

where $M_{R22} = 86.47$ g.mol^{-1} is the molar mass of R22 and, $T = 293$ K and $p = 101325$ Pa are the temperature and pressure chosen as the initial conditions ahead of the shock wave.

Periodic boundary conditions are used to model the upper and lower shock-tube walls which are spaced by 89 mm. Radiation conditions are imposed at the upstream and downstream boundaries of the shock-tube [60]. Four uniform grids, containing 100, 200, 400 and 800 mesh cells in the initial bubble radius R_0, denoted by R_0100, R_0200, R_0400 and R_0800, respectively, are considered. The number of mesh cells in the x and y directions, are collected in Table 2. The numerical time step is related to the CFL number, which is, based on the highest speed of sound of the flow c_{max}, given by $CFL = c_{max}\Delta t/\Delta x = 0.9$. For the helium bubble, the speed of sound in the helium–air mixture $c_{ha} = 869$ m.s^{-1} is the maximum speed of sound. In the case of the R22 bubble, the speed of sound in air $c_{air} = 366.3$ m.s^{-1} is employed to determine the time step Δt. Both cases are simulated using the discontinuity-capturing methodology introduced in Section 3.4.

In order to consider the same initial conditions for the four meshes, the thicknesses of the interface and the shock wave are fixed using the hyperbolic tangent profile of equation (32). The thicknesses are arbitrary set to $3\Delta x$ on the grid R_0100. Thus, they are equal to $6\Delta x$, $12\Delta x$ and $24\Delta x$ on the meshes R_0200, R_0400 and R_0800, respectively. The hyperbolic tangent profile is used to define the interface on the viscosities, conductivities, density and $1/(\gamma - 1)$, and the shock wave on density, axial velocity and pressure. Note that simulations have also been performed for a very thin interface and shock wave, which resulted in solutions similar to those obtained for the present thick interfaces.

5.2.2. Helium bubble

The solutions obtained at $t = 32$, 82, 102, 245, 427 and 674 µs for the helium bubble using the mesh R_0200 are shown in Fig. 16. The time $t = 0$ corresponds to the moment of the first contact between the shock wave and the bubble interface. The numerical results are presented in the lower-half pictures and are compared with the experimental shadow-photographs in

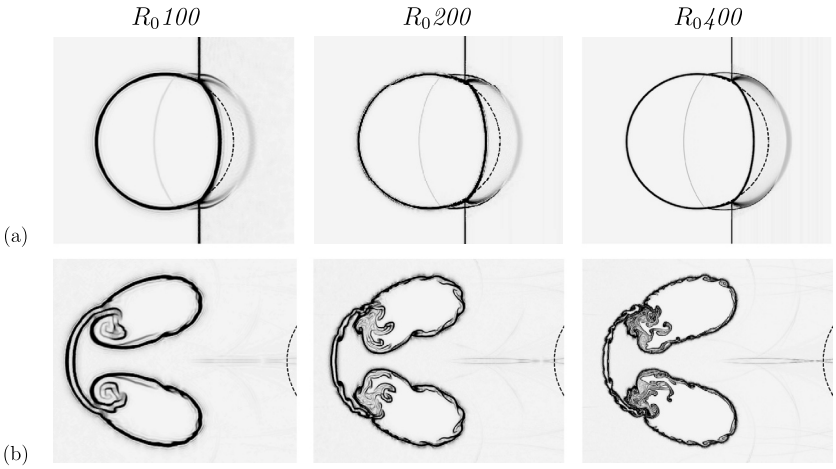

Fig. 17. Helium bubble: numerical Schlieren pictures obtained at time (a) $t = 32$ µs and (b) $t = 674$ µs using the meshes R_0100 (first column), R_0200 (second column) and R_0400 (third column).

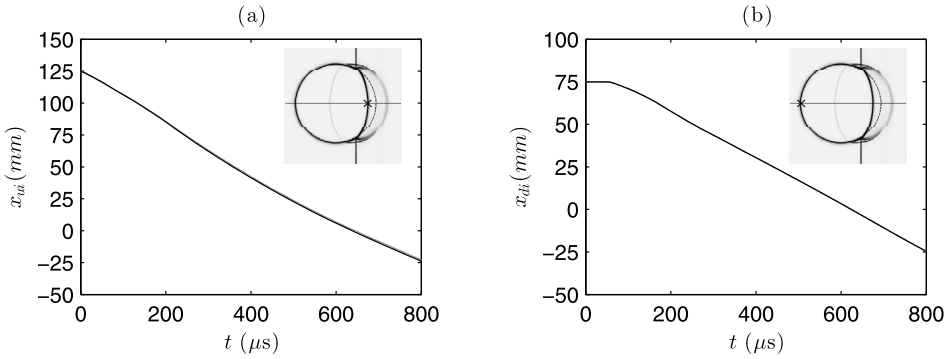

Fig. 18. Helium bubble: temporal variations of the positions of the (a) upstream and (b) downstream sides of the interface obtained using —— R_0100, - - - R_0200 and —— R_0400. These positions are indicated by x in the upper-right figures.

the upper-half pictures [24]. The numerical solutions represent artificial Schlieren fields, defined as the norm of the density gradient $|\nabla\rho|$ [21,49,57]. The dashed circle indicates the initial position of the bubble.

In Fig. 16(a), the upstream side of the interface is flattened due to the impact of the shock wave. Three pressure waves appear: a reflected wave propagating through air in the upstream direction, a refracted wave travelling downstream inside the bubble, and the incident shock wave propagating downstream, above and below the bubble. In Fig. 16(b), the bubble has moved slightly downstream. As the speed of sound is higher in helium than in air, the refracted wave is out of the bubble whereas the shock wave is still located above and below the bubble. Finally, in Figs. 16(d–f), the upstream side of the interface penetrates the bubble, leading to a bubble of kidney shape which then deforms. The overall behaviour has been analysed in prior work in terms of baroclinic instability, reviewed in [50]. The pressure waves are not exactly at the same positions on the numerical and experimental pictures. However, the bubble deformations are consistent at all times.

The Schlieren pictures obtained in the simulations using the three meshes R_0100, R_0200 and R_0400 at time $t = 32$ and 674 µs are presented in Fig. 17. At the first time in Fig. 17(a), no significant difference is observed between the solutions. The black lines indicative of strong density gradients are thinner on the finest mesh than on the two other meshes. Therefore, the discontinuities are thinner as the mesh is finer. At the second time in Fig. 17(b), the shapes of the bubble are similar but the small structures developing on the interface are better resolved on the meshes R_0200 and R_0400.

The temporal variations of the positions of the upstream and downstream sides of the interface x_{ui} and x_{di}, respectively, are presented in Figs. 18(a) and 18(b). These positions are estimated along the x-direction on the centreline of the domain, and correspond to the location where the volume fraction is equal to 0.5. The solutions in gray, gray dashed and black lines are obtained using the grids R_0100, R_0200 and R_0400, respectively. In Fig. 18(a), the position x_{ui} decreases monotonically during the whole simulation whereas in Fig. 18(b), the location x_{di} is constant up to $t = 54$ µs and then decreases. These results are due to the fact that the shock wave hits the upstream side of the interface at $t = 0$, and the downstream side of the interface starts to move downstream after its interaction with the refracted wave propagating in the bubble at $t = 54$ µs. In above all, no significant differences are observed between the solutions obtained using the different grids. Therefore, the present results appear to be converged with respect to the grid.

Table 3
Helium bubble: mean velocities of the incident shock u_s, the refracted wave u_r, the transmitted wave u_t, and the upstream and downstream sides of the interface u_{ui} and u_{di}, obtained using R_0400.

	u_s (m.s^{-1})	u_r (m.s^{-1})	u_t (m.s^{-1})	u_{ui} (m.s^{-1})	u_{di} (m.s^{-1})
Experiment [24]	410 ± 41	900 ± 90	393 ± 39.3	170 ± 17	145 ± 14.5
Simulation	417	948.7	377	181.7	139.5

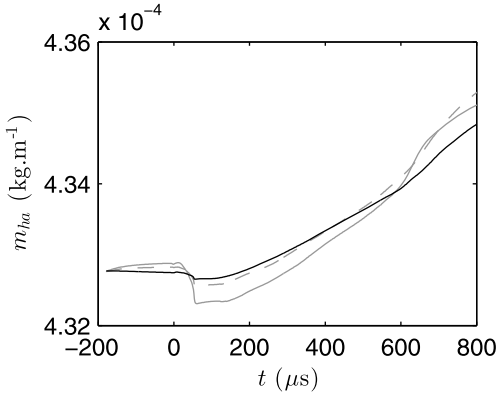

Fig. 19. Helium bubble: temporal variations of the mass m_{ha}: solutions obtained using —— R_0100, - - - R_0200 and —— R_0400.

The mean velocities of the different pressure waves obtained using R_0400 are compared with experimental results in Table 3. They are estimated along the x-direction on the centreline of the domain. The velocity u_s of the incident shock is computed from the start of the simulation at time $t = -180$ µs, up to shock-bubble impact at $t = 0$. The velocity u_r of the refracted wave is estimated during its propagation inside the bubble. The transmitted wave propagates downstream of the bubble in air at speed u_t. Finally, the velocities of motion of the upstream and downstream sides of the interface are denoted by u_{ui} and u_{di}, respectively. The numerical results are roughly comparable to the measurements. The speed of the refracted wave in the simulation is 948 m.s^{-1}, which is higher than in the experiment but similar to value of 945 m.s^{-1} provided by the simulation of Coralic and Colonius [15]. The difference in speed of the refracted waves in the experiment and the simulation can be seen in Fig. 16(a), where the waves on the upper-half and the lower-half pictures do not exactly coincide. Since the properties of the helium–air mixture significantly affect the wave propagation in the bubble, it is possible that the mass concentration of air contained inside the bubble is higher than was estimated experimentally.

In order to verify that the numerical methods conserve mass, the mass of the helium–air mixture m_{ha} contained inside the bubble is estimated by integrating the density over the surface of the bubble S as

$$m_{ha} = \iint_S \rho \, dxdy.$$

In practice, since the bubble surface is unknown, the mass of the bubble is calculated from the product of the mass fraction of the helium–air mixture Y_{ha} with density. This product is integrated over the computational domain Σ, leading to

$$m_{ha} = \iint_\Sigma Y_{ha} \rho \, dxdy. \tag{33}$$

The temporal variations of the mass m_{ha} obtained using the grids R_0100, R_0200 and R_0400 are presented in Fig. 19. The bubble mass is nearly constant before the contact between the shock and the interface at $t = 0$. It decreases slightly just afterwards, at a rate that is weaker using a finer mesh. At later times, the mass monotonically increases using the three grids. It should be kept in mind that during this simulation the bubble is much deformed physically. In spite of this, the maximal variation in the bubble mass remains small, at most 0.5%. Note that similar results were obtained when starting with a thinner initial interface.

The present results indicate that the variations of the bubble mass here depend appreciably neither on the grid nor on the initial interface thickness. Therefore, the small error in mass can be attributed to the use of the quantity $1/(\gamma - 1)$ as the advected variable, which has been motivated in Section 4. In order to reduce this error one possibility could be to include a dilatational source term in the volume fraction equation as in Beig and Johnsen [7].

5.2.3. R22 bubble

The results obtained at $t = 55$, 115, 135, 187, 247 and 417 µs for the R22 bubble using the mesh R_0200 are shown in Fig. 20. They are compared with experimental shadow-photographs. In Figs. 20(a–b), the refracted wave travelling inside the

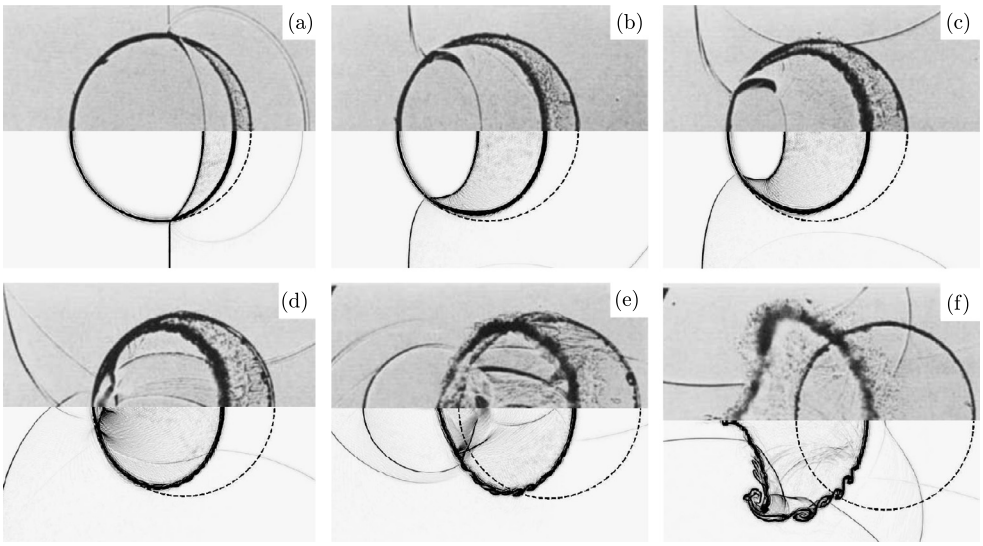

Fig. 20. R22 bubble: numerical Schlieren pictures (lower-half pictures) and experimental shadow-photographs (upper-half pictures) [24] obtained at (a) $t = 55$ µs, (b) $t = 115$ µs, (c) $t = 135$ µs, (d) $t = 187$ µs, (e) $t = 247$ µs and (f) $t = 417$ µs.

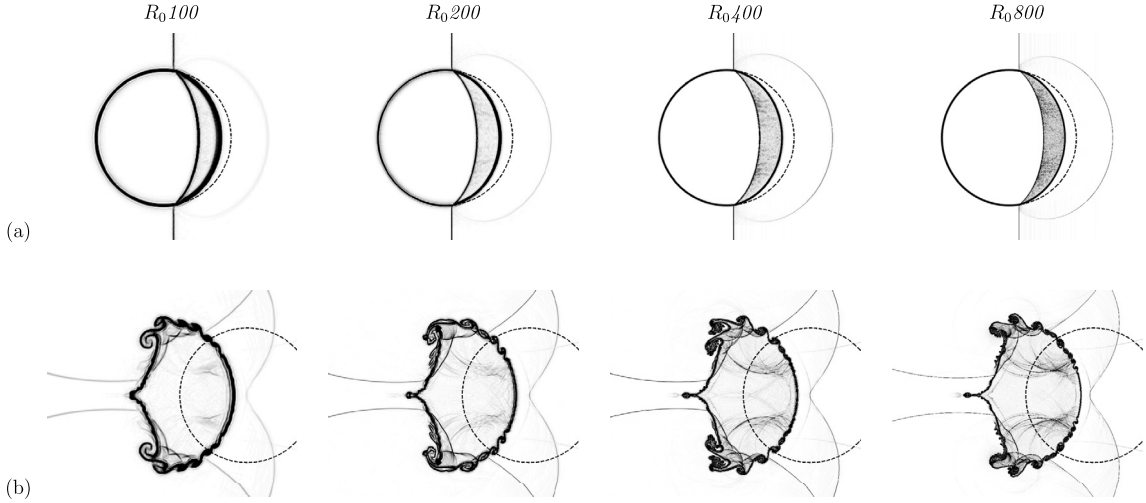

Fig. 21. R22 bubble: numerical Schlieren pictures obtained at (a) $t = 55$ µs and (b) $t = 417$ µs using the meshes R_0100 (first column), R_0200 (second column), R_0400 (third column) and R_0800 (fourth column).

bubble is seen to propagate more slowly than the incident shock in air. Consequently, in Fig. 20(c), the refracted wave is still in the bubble, while the incident shock is already downstream of the bubble. At later times, in Figs. 20(e–f), the refracted wave is out of the bubble, generating the transmitted wave. In addition, the bubble has slightly moved downstream, and the downstream side of the interface penetrates into the bubble resulting in a spike on the bubble axis. The interfacial layer appears to roll up, as can be expected from baroclinically-generated vorticity in the interfacial layer [50]. This instability is clearly observed in the simulation but the experimental images appear unclear at this stage. It has been noticed also in the numerical work of Hejazialhosseini et al. [25], So et al. [57] and Daude et al. [17]. This may appear blurred on the shadow-photographs because of the view along the spanwise direction of the cylindrical bubble, which is 8.8 cm long. Furthermore, due to the sensitivity of this behaviour to the initial interface thickness [57], its development may be affected by the solid membrane.

The numerical Schlieren pictures obtained at $t = 55$ and 417 µs using R_0100, R_0200, R_0400 and R_0800 are presented in Fig. 21. At the first time in Fig. 21(a), the bubble shape is the same in the four cases. On the finest mesh, the density gradients are represented by thinner black lines than on the coarsest grid. Therefore, the density discontinuities at the interface and the shock wave are sharper on the mesh R_0800 than on the three others. At the second time, in Fig. 21(b), the acoustic waves inside and outside the bubble, and the small vortices developing on the bubble interface are better resolved

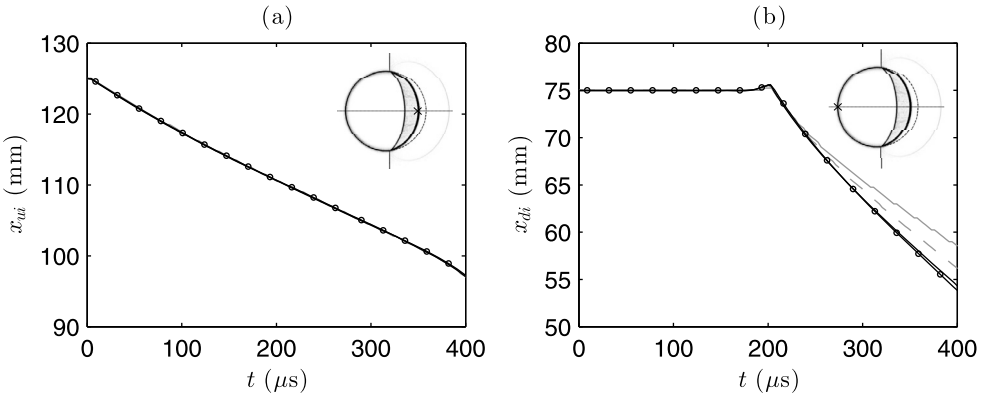

Fig. 22. R22 bubble: temporal variations of the positions of the (a) upstream and (b) downstream sides of the interface obtained using —— R_0100, - - - R_0200, —— R_0400 and —●— R_0800. These positions are indicated by x in the upper-right figures.

Table 4
R22 bubble: mean velocities of the incident shock u_s, the refracted wave u_r, the transmitted wave u_t, and the upstream and downstream sides of the interface u_{ui} and u_{di}, obtained using R_0400.

	u_s (m.s^{-1})	u_r (m.s^{-1})	u_t (m.s^{-1})	u_{ui} (m.s^{-1})	u_{di} (m.s^{-1})
Experiment [24]	410 ± 41	240 ± 24	540 ± 54	73 ± 11	78 ± 8
Simulation	417	250.5	524	73.7	79.4

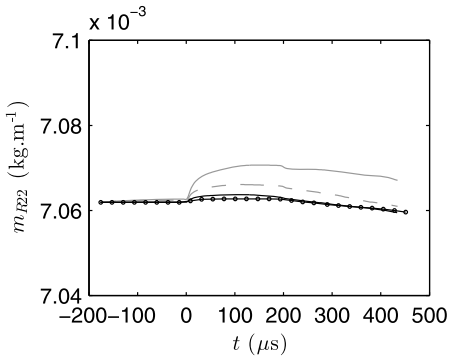

Fig. 23. R22 bubble: temporal variations of mass m_{R22}: solutions obtained using —— R_0100, - - - R_0200, —— R_0400 and —●— R_0800.

using the finest grid. Furthermore, the spike generated on the downstream side of the interface does not appear using the mesh R_0100.

As for the helium bubble, the temporal variations of the positions of the upstream and downstream sides of the interface are presented in Figs. 22(a) and 22(b). The solutions are obtained using the grids R_0100, R_0200, R_0400 and R_0800. In Fig. 22(a), the position x_{ui} decreases monotonically and no differences are observed between the four solutions. In Fig. 22(b) the location x_{di} is constant up to $t = 200$ µs and then decreases. After $t = 200$ µs, the results obtained using the grids R_0100, R_0200 and R_0400 differ but those obtained using R_0400 and R_0800 are very similar. The differences can be attributed to the formation of a spike on the bubble axis at $t = 200$ µs when the refracted wave hits the downstream side of the interface. This spike is indeed longer on the finest grids than on the coarsest. However, a number of 400 mesh cells in the bubble radius allows the spike length to be correctly predicted.

The mean velocities of the shock wave, the refracted wave, the transmitted wave, and the mean velocities of the upstream and downstream sides of the interface obtained using R_0400 are given in Table 4. They are similar to the experimental results, also given in Table 4. Thus, the interface deformations and the propagation of the pressure waves inside and outside the bubble are both very well simulated.

In the same way as for the helium bubble, the mass of the R22 bubble m_{R22} is computed. The temporal variations of m_{R22} obtained using the three meshes are presented in Fig. 23. The variations are negligible before the shock/interface contact, from $t = -180$ µs up to $t = 0$. Then, when the shock hits the interface, the mass increases slightly. Subsequently, the mass monotonically decreases for the three grids yielding a maximal error of 0.025% compared to the initial bubble mass. Therefore, the mass variations are of small magnitude despite the large deformation of the bubble.

Table 5
Constants of Sutherland's equation (34) used to calculate the shear viscosity of air, SF6, helium and R22.

	$\mu(T_0)$ (kg.m^{-1}.s^{-1})	T_0 (K)	S (K)
Air	1.716×10^{-5}	273	130
SF6	1.4×10^{-5}	273	227
He	1.87×10^{-5}	273	65
R22	1.289×10^{-5}	300.5	310

6. Conclusion

A computational method is proposed here for the simulation of compressible viscous gas–gas flows. It consists in solving the single-fluid formulation of the Navier–Stokes equations associated with an advection equation governing the interface. These equations are solved using explicit high-order centred finite difference schemes. A sixth-order selective filter is applied to remove grid-to-grid oscillations and a discontinuity-capturing methodology, including shock-sensors and an adaptive spatial filter enabling the capture of various discontinuities such as, shock waves and deformable interfaces is employed. The choice of the advected variable governing the interface displacements appears to be very important to reduce numerical errors.

It is shown that the present algorithm is suitable for the simulations of interactions between shock waves and interfaces including viscous effects and thermal conduction. These interactions lead to the generation of various pressure waves such as transmitted and refracted waves. They are all captured using the same discontinuity-capturing methodology which removes Gibbs' oscillations while conserving discontinuity sharpness. Slight differences are noticed between numerical and experimental results. They are probably caused by differences in initial conditions between simulation and experiments. Furthermore, the deformation of the interface is well predicted, and the high-order schemes allow us to obtain converged results using relatively coarse meshes.

Acknowledgements

This work was performed using HPC resources of P2CHPD (Pôle de Calcul Hautes Performances Dédiés) of Université Lyon 1 (Mésocentre FLMSN). This work was performed within the framework of the Labex CeLyA of Université de Lyon operated by the French National Research Agency (ANR). PDMS gratefully acknowledges Dr Stephen J. Shaw of Xi'an Jiaotong-Liverpool University for useful discussions.

Appendix A. Viscosity and thermal conductivity calculation

The shear viscosity μ, the bulk viscosity μ_b and the thermal conductivity λ are estimated using empirical relations, as functions of temperature. The shear viscosity is computed from Sutherland's equation [59],

$$\mu = \mu(T_0)\left(\frac{T_0+S}{T+S}\right)\left(\frac{T}{T_0}\right)^{(3/2)}, \tag{34}$$

where T_0 is a reference temperature and S is a constant, given in Table 5. These values are taken from Hellemans et al. [26] and Johnston [35] for air, from references [64] for SF6, [3,38] for helium and [36,39] for R22.

Stokes' hypothesis, consisting in neglecting the bulk viscosity μ_b with respect to μ, is true for dilute monoatomic gases. Therefore, the helium bulk viscosity is equal to zero. However, this is not the case for most other gases (and liquids) [23]. Bulk viscosity has an effect on the damping and the thickness of shock waves [19]. The bulk viscosities of air and SF6 are estimated using empirical relations. The air bulk viscosity is computed from the relation proposed by Rossing [52] $\mu_{b_{air}} = 0.6\mu_{air}$, where μ_{air} is the shear viscosity of air obtained from Sutherland's equation (34). The thermal evolution of the SF6 bulk viscosity [16], is given by

$$\mu_{b_{SF6}} = 7.54 \times 10^{-5}\left(0.2064(\gamma_{SF6}-1)^2 \exp\left(\frac{121}{T^{1/3}} - \frac{339}{T^{2/3}}\right)\right).$$

Since no information has been found on the bulk viscosity of R22 gas, this has been set to zero.

Similarly, the thermal conductivities of air, SF6, helium and R22 are expressed as functions of temperature. The air thermal conductivity λ_{air} is determined from the Prandtl number Pr, as

$$\lambda_{air} = \frac{\mu_{air} c_{p,air}}{Pr} \tag{35}$$

using $Pr = 0.7$ and $c_{p,air} = \gamma_{air} c_{v,air}$ is the air heat capacity at constant pressure, obtained from the air heat capacity at constant volume $c_{v,air} = 717.5$ J.kg^{-1}.K^{-1}.

A second-order polynomial approximation issued from experimental measurements [63] is used to compute the thermal conductivity of SF6 as

$$\lambda_{SF6} = -7.3447 \times 10^{-8} T^2 + 1.2882 \times 10^{-4} T - 1.9136 \times 10^{-2}\,. \tag{36}$$

The helium thermal conductivity λ_h is estimated using a third-order polynomial [51]

$$\lambda_h = 1.29 \times 10^{-11} T^3 - 7.45 \times 10^{-8} T^2 + 3.896 \times 10^{-4} T + 3.722 \times 10^{-2}. \tag{37}$$

Finally, the R22 thermal conductivity λ_{R22} is obtained using a linear fit of experimental data [36]. It is expressed as:

$$\lambda_{R22} = 6.227 \times 10^{-5} T - 7.6001 \times 10^{-3}. \tag{38}$$

References

[1] R. Abgrall, How to prevent pressure oscillations in multicomponent flow calculations: a quasi conservative approach, J. Comput. Phys. 125 (1996) 150–160.
[2] R. Abgrall, S. Karni, Computations of compressible multifluids, J. Comput. Phys. 169 (2) (2001) 594–623.
[3] S.W. Akin, Thermodynamic properties of helium, Trans. Am. Soc. Mech. Eng. 72 (1950) 751–757.
[4] G. Allaire, S. Clerc, S. Kokh, A five-equation model for the simulation of interfaces between compressible fluids, J. Comput. Phys. 181 (2) (2002) 577–616.
[5] J.D. Anderson, Modern Compressible Flow: With Historical Perspective, vol. 12, McGraw-Hill, New York, 1990.
[6] David Arnett, The role of mixing in astrophysics, Astrophys. J. Suppl. Ser. 127 (2) (2000) 213.
[7] S.A. Beig, E. Johnsen, Maintaining interface equilibrium conditions in compressible multiphase flows using interface capturing, J. Comput. Phys. 302 (2015) 548–566.
[8] C. Bogey, C. Bailly, A family of low dispersive and low dissipative explicit schemes for flow and noise computations, J. Comput. Phys. 194 (2004) 194–214.
[9] C. Bogey, N. De Cacqueray, C. Bailly, A shock-capturing methodology based on adaptative spatial filtering for high-order non-linear computations, J. Comput. Phys. 228 (2009) 1447–1465.
[10] C. Bogey, R. Gojon, Feedback loop and upwind-propagating waves in ideally expanded supersonic impinging round jets, J. Fluid Mech. 823 (2017) 562–591.
[11] C. Bogey, O. Marsden, C. Bailly, Effects of moderate Reynolds numbers on subsonic round jets with highly disturbed nozzle-exit boundary layers, Phys. Fluids 24 (10) (2012) 105107.
[12] J.U. Brackbill, D.B. Kothe, C. Zemach, A continuum method for modeling surface tension, J. Comput. Phys. 100 (1992) 335–354.
[13] M. Brouillette, The Richtmyer–Meshkov instability, Annu. Rev. Fluid Mech. 34 (1) (2002) 445–468.
[14] Y.C. Chang, T.Y. Hou, B. Merriman, S. Osher, A level set formulation of Eulerian interface capturing methods for incompressible fluid flows, J. Comput. Phys. 124 (1996) 449–464.
[15] V. Coralic, T. Colonius, Finite-volume WENO scheme for viscous compressible multicomponent flows, J. Comput. Phys. 274 (2014) 95–121.
[16] M.S. Cramer, Numerical estimates for the bulk viscosity of ideal gases, Phys. Fluids 24 (2012).
[17] F. Daude, P. Galon, Z. Gao, E. Blaud, Numerical experiments using a HLLC-type scheme with ALE formulation for compressible two-phase flows five-equation models with phase transition, Comput. Fluids 94 (2014) 112–138.
[18] N. de Cacqueray, C. Bogey, C. Bailly, Investigation of a high-mach-number overexpanded jet using large-eddy simulation, AIAA J. 49 (10) (2011) 2171–2182.
[19] G. Emanuel, B.M. Argrow, Linear dependence of the bulk viscosity on shock wave thickness, Phys. Fluids (1994-present) 6 (9) (1994) 3203–3205.
[20] T. Gallouët, J.-M. Hérard, N. Seguin, Some recent finite volume schemes to compute Euler equations using real gas EOS, Int. J. Numer. Methods Fluids 39 (12) (2002) 1073–1138.
[21] J. Giordano, Y. Burtschell, Richtmyer–Meshkov instability induced by shock-bubble interaction: numerical and analytical studies with experimental validation, Phys. Fluids 18 (3) (2006) 036102.
[22] J. Glimm, E. Isaacson, D. Marchesin, O. McBryan, Front tracking for hyperbolic systems, Adv. Appl. Math. 2 (1) (1981) 91–119.
[23] R.E. Graves, B.M. Argrow, Bulk viscosity: past to present, J. Thermophys. Heat Transf. 13 (3) (1999) 337–342.
[24] J-F. Haas, B. Sturtevant, Interaction of weak shock waves with cylindrical and spherical gas inhomogeneities, J. Fluid Mech. 181 (1987) 41–76.
[25] B. Hejazialhosseini, D. Rossinelli, M. Bergdorf, P. Koumoutsakos, High order finite volume methods on wavelet-adapted grids with local time-stepping on multicore architectures for the simulation of shock-bubble interactions, J. Comput. Phys. 229 (22) (2010) 8364–8383.
[26] J.M. Hellemans, J. Kestin, S.T. Ro, The viscosity of oxygen and of some of its mixtures with other gases, Physica 65 (2) (1973) 362–375.
[27] M. Herrmann, P. Moin, S.I. Abarzhi, Nonlinear evolution of the Richtmyer–Meshkov instability, J. Fluid Mech. 612 (2008) 311–338.
[28] X.Y. Hu, B.C. Khoo, N.A. Adams, F.L. Huang, A conservative interface method for compressible flows, J. Comput. Phys. 219 (2) (2006) 553–578.
[29] J.M. Hyman, Numerical methods for tracking interfaces, Phys. D: Nonlinear Phenom. 12 (1) (1984) 396–407.
[30] J.W. Jacobs, V.V. Krivets, Experiments on the late-time development of single-mode Richtmyer–Meshkov instability, Phys. Fluids (2005) 034105.
[31] J.W. Jacobs, V.V. Krivets, Personal communication.
[32] E. Johnsen, T. Colonius, Implementation of WENO schemes in compressible multicomponent flow problems, J. Comput. Phys. 219 (2006) 715–732.
[33] E. Johnsen, T. Colonius, Numerical simulations of non-spherical bubble collapse, J. Fluid Mech. 629 (2009) 231–262.
[34] E. Johnsen, F. Ham, Preventing numerical errors generated by interface-capturing schemes in compressible multi-material flows, J. Comput. Phys. 231 (17) (2012) 5705–5717.
[35] H.L. Johnston, K.E. McCloskey, Viscosities of several common gases between 90° K. and room temperature, J. Phys. Chem. 44 (9) (1940) 1038–1058.
[36] S. Kandlikar, C. Bijlani, S. Sukhatme, Predicting the properties of mixtures of R22 and R12 part II-transport properties, ASHRAE 2343 (1975).
[37] M. Kang, R.P. Fedkiw, X.-D. Liu, A boundary condition capturing method for multiphase incompressible flow, J. Sci. Comput. 15 (2000) 323–360.
[38] J. Kestin, W. Leidenfrost, The viscosity of helium, Physica 25 (1–6) (1959) 537–555.
[39] J. Kestin, W.A. Wakeham, The viscosity of three polar gases, Ber. Bunsenges. Phys. Chem. 83 (6) (1979) 573–576.
[40] J.W. Kim, D.J. Lee, Adaptive nonlinear artificial dissipation model for computational aeroacoustics, AIAA J. 39 (5) (2001) 810–818.
[41] F. Kremer, C. Bogey, Large-eddy simulation of turbulent channel flow using relaxation filtering: resolution requirement and Reynolds number effects, Comput. Fluids 116 (2015) 17–28.
[42] M. Latini, O. Schilling, W.S. Don, Effects of weno flux reconstruction order and spatial resolution on reshocked two-dimensional Richtmyer–Meshkov instability, J. Comput. Phys. 221 (2) (2007) 805–836.

[43] G. Layes, G. Jourdan, L. Houas, Experimental study on a plane shock wave accelerating a gas bubble, Phys. Fluids 21 (7) (2009) 074102.
[44] E. Maitre, Review of numerical methods for free interfaces, Les Houches 27 (2006) 31.
[45] Frank E. Marble, Gavin J. Hendricks, Edward E. Zukoski, Progress toward shock enhancement of supersonic combustion processes, in: Turbulent Reactive Flows, Springer, 1989, pp. 932–950.
[46] O. Marsden, C. Bogey, C. Bailly, A study of infrasound propagation based on high-order finite difference solutions of the Navier–Stokes equations, J. Acoust. Soc. Am. 135 (3) (2014) 1083–1095.
[47] S. Nagrath, K. Jansen, R.T. Lahey, I. Akhatov, Hydrodynamic simulation of air bubble implosion using a level set approach, J. Comput. Phys. 215 (1) (2006) 98–132.
[48] S. Osher, R. Fedkiw, Level Set Methods and Dynamic Implicit Surfaces, vol. 153, Springer Science & Business, Media, 2003.
[49] J.J. Quirk, S. Karni, On the dynamics of a shock-bubble interaction, J. Fluid Mech. 318 (1996) 129–163.
[50] D. Ranjan, J. Oakley, R. Bonazza, Shock-bubble interactions, Annu. Rev. Fluid Mech. 43 (2011) 117–140.
[51] R.C. Reid, J.M. Prausnitz, B.E. Poling, The Properties of Gases and Liquids, 1987.
[52] T.D. Rossing, Springer Handbook of Acoustics, Springer, 2007.
[53] R. Saurel, P. Bovin, O. Le Metayer, A general formulation for cavitating, boiling and evaporating flows, Comput. Fluids 128 (2016) 53–64.
[54] R. Saurel, F. Petitpas, R.A. Berry, Simple and efficient relaxation methods for interfaces separating compressible fluids, cavitating flows and shocks in multiphase mixtures, J. Comput. Phys. 228 (2) (2009) 1678–1712.
[55] R. Scardovelli, S. Zaleski, Direct numerical simulation of free-surface and interfacial flow, Annu. Rev. Fluid Mech. 31 (1) (1999) 567–603.
[56] K-M. Shyue, An efficient shock-capturing algorithm for compressible multicomponent problems, J. Comput. Phys. 142 (1998) 208–242.
[57] K.K. So, X.Y. Hu, N.A. Adams, Anti-diffusion interface sharpening technique for two-phase compressible flow simulations, J. Comput. Phys. 231 (11) (2012) 4304–4323.
[58] Z. Solomenko, P.D.M. Spelt, L.Ó. Náraigh, P. Alix, Mass conservation and reduction of parasitic interfacial waves in level-set methods for the numerical simulation of two-phase flows: a comparative study, Int. J. Multiph. Flow (95) (2017) 235–256.
[59] W. Sutherland, The viscosity of gases and molecular force, Lond. Edinb. Dublin Philos. Mag. J. Sci. 36 (223) (1893) 507–531.
[60] C.K.W. Tam, Z. Dong, Radiation and outflow boundary conditions for direct computation of acoustic and flow disturbances in a non uniform mean flow, J. Comput. Acoust. 4 (1996) 175–201.
[61] V.K. Tritschler, X.Y. Hu, S. Hickel, N.A. Adams, Numerical simulation of a Richtmyer–Meshkov instability with an adaptive central-upwind sixth-order WENO scheme, Phys. Scr. 2013 (T155) (2013) 014016.
[62] G. Tryggvason, B. Bunner, A. Esmaeeli, D. Juric, N. Al-Rawahi, W. Tauber, J. Han, S. Nas, Y-J. Jan, A front-tracking method for the computations of multiphase flow, J. Comput. Phys. 169 (2) (2001) 708–759.
[63] F.J. Uribe, E.A. Mason, J. Kestin, Thermal conductivity of nine polyatomic gases at low density, J. Phys. Chem. Ref. Data 19 (5) (1990) 1123–1136.
[64] J. Wilhelm, D. Seibt, E. Bich, E. Vogel, E. Hassel, Viscosity measurements on gaseous sulfur hexafluoride, J. Chem. Eng. Data 50 (3) (2005) 896–906.